



Projectile Impact on Plain and Reinforced Concrete Slabs

Øystein E. K. Jacobsen^{1,2} · Martin Kristoffersen^{1,2} · Sumita Dey³ · Tore Børvik^{1,2,3}

Received: 6 October 2022 / Accepted: 3 May 2023
© The Author(s) 2023

Abstract

Reinforced concrete is a material frequently used in protective structures and infrastructure exposed to extreme loading. In this study, the ballistic perforation resistance of 100 mm thick plain and reinforced concrete slabs impacted by 20 mm ogive-nose steel projectiles was investigated both experimentally and numerically. Two different reinforcement configurations were used to investigate the effect of rebar diameter and spacing. Concrete with nominal unconfined compressive strength of 75 MPa was used to cast material test specimens and slabs. Ballistic impact tests were performed in a compressed gas gun facility. The mechanical properties of the concrete were found using standardised tests and two-dimensional digital image correlation, and the constitutive relation was described by a modified version of the Holmquist-Johnson-Cook model. Finite element models in LS-DYNA reproduced the projectile residual velocity in good agreement with the experimental results. The primary objective of the study was thus to validate a rather simple constitutive relation intended for large scale numerical simulations of concrete structures exposed to ballistic impact loading, while a secondary objective was to investigate the effect of reinforcement on the ballistic perforation resistance of concrete slabs both experimentally and numerically since the literature is somewhat inconsistent on this matter.

Keywords Reinforced concrete · Material tests · Ballistic impact · LS-DYNA simulations

Introduction

Concrete is by far the most used construction material in the world. Of all materials, only water exceeds the consumption of concrete [1]. Owing to its high compressive strength, durability and abundance, concrete is used for almost any type of structure – ranging from critical infrastructure to military fortifications. In either case, it is vital to understand how a complex composite material like concrete behaves when subjected to extreme and potentially devastating loads like explosions or ballistic impact. Thus, numerous studies on concrete targets subjected to impact loading can be found in the open literature [2–7]. Studies like these typically

involve experimental works, analytical and/or empirical formulations, numerical studies, or any combination of these. Ballistic impact studies on concrete are usually separated into studies on semi-infinite slabs and slabs with a finite thickness. The former investigate depth of penetration into massive concrete structures, while the latter examine perforation of concrete slabs. This study is of the latter kind, where a special emphasis is put on the effect of conventional steel reinforcement.

A common and reasonable assumption in many studies modelling concrete, is to treat the concrete as a homogeneous solid rather than the porous composite material it actually is. When reinforcement is introduced to increase the tensile capacity, this assumption is either abandoned or kept depending on the type of reinforcement used. Fibre reinforcement may be assumed roughly evenly distributed and can then be accounted for in the constitutive relation [8]. Conventional grid reinforcement have specific locations in the composite structure and should thus be modelled explicitly and separately from the concrete [9, 10]. There is extensive literature on the effect of reinforcement on ballistic performance for concrete targets subjected to impact loading, and studies on different types of

✉ Øystein E. K. Jacobsen
oystein.e.k.jacobsen@ntnu.no

¹ Structural Impact Laboratory (SIMLab), Department of Structural Engineering, NTNU – Norwegian University of Science and Technology, NO-7491 Trondheim, Norway

² Centre for Advanced Structural Analysis (CASA), NTNU, NO-7491 Trondheim, Norway

³ Research and Development Department, Norwegian Defence Estates Agency, Oslo, Norway

reinforcement can be found in the open literature, e.g., grid reinforcement [2, 11–13], fibre reinforcement [14, 15], ferrocement [16], wire mesh [17] and prestressed concrete [18]. Some studies on the effect of reinforcement on ballistic perforation resistance are presented in the following.

In the early 1990s, Hanchak et al. [2] performed experiments on 178 mm thick reinforced concrete (RC) slabs with unconfined compressive strengths of 48 and 140 MPa, and found that striking the reinforcement had negligible effect for projectiles with striking velocity of 750 m/s and mass 0.50 kg. Note that only one of the tests had direct contact between projectile and rebar, with a velocity well above the ballistic limit, i.e., the lowest velocity where the projectile perforates the slab with zero residual velocity. They also examined how the concrete strength affected the ballistic perforation resistance, and speculated that the penetration resistance in the crater regions was insensitive to unconfined compressive strength.

Abdel-Kader and Fouda [17] performed an extensive study on ballistic perforation of 100 mm thick plain slabs and slabs with different reinforcement configurations. Using projectiles with diameter 23 mm and mass 0.175 kg, they found no significant effect on the ballistic performance when adding a reinforcement mesh with reinforcement ratio 0.8 %. However, they observed that the residual velocity of the projectile decreased when the reinforcement was struck, but only through one test with direct contact between the projectile and the rebars. They also pointed out that considerable scatter should be expected when studying RC slabs.

Dancygier et al. [3] performed impact tests on both normal and high strength concrete reinforced with either steel fibres or steel grid bars. They found that different types of reinforcement can enhance the ballistic resistance, mainly by limiting the damaged area. They also found that the amount of reinforcing steel had almost no effect on the perforation resistance, and only some effect on reducing the rear face damaged area for relatively high reinforcement volumes.

In a study on thinner slabs, Dancygier [12] found that increasing the reinforcement ratio enhanced the performance against perforation. The 50–60 mm thick slabs were impacted by projectiles with mass 0.165 kg. Similar results were found when Rajput et al. and Rajput and Iqbal [11, 18] compared plain and reinforced concrete slabs subjected to impact loading through experimental tests and numerical simulations in ABAQUS/Explicit. They also found that the reinforced slabs had increased ballistic capacity. Additionally, they found that prestressing stimulated globalisation of the deformation and thus enhanced the ballistic resistance of the target. A significant decrease in the scabbing area, i.e., mass ejected from the back of the slab, for the reinforced slabs was also found, and lower scabbing was observed for lower striking velocities. Prestressing the concrete both increased the ballistic limit velocity, and decreased scabbing

and spalling (mass ejected on front side of the slab) significantly, with less clear effects observed for conventional reinforced and plain concrete.

When comparing the presented studies, it seems that the literature is somewhat inconsistent with respect to the effect of grid reinforcement on the ballistic perforation resistance in concrete slabs.

Furthermore, there are several studies where the effect of concrete target thickness on ballistic perforation resistance has been studied. Shiu et al. [19] performed discrete element simulations in YADE [20] on ballistic impact on concrete. They used simple compression tests and hydrostatic tests to calibrate material behaviour, and argued that compaction was a minor part of the perforation process for thin slabs, where tensile fracture was the major component. Simulation of a slab with a higher ratio between slab thickness and projectile diameter showed differently distributed compaction, which was more intense closer to the missile head.

Li et al. [21] studied slabs with thicknesses in the range of 80 mm to 110 mm subjected to armour-piercing ammunition and found that the damage of the thinner slabs was more severe, both for spalling and scabbing sizes. For the thicker slabs, they saw less damage, and attributed this effect to better confinement. They argued that the impact resistance can be enhanced with confinement, which can decrease the damage degree.

Several constitutive models have been developed for dynamic loading of concrete. Detailed material characterisation of concrete is a difficult task due to the brittleness, inherent heterogeneity, microcracking and in general complex behaviour of the material [22]. It is thus common to assume that the composite material is a homogeneous solid for simplicity [23]. Some frequently used homogenised models are the K&C model [8, 23], the RHT model [24, 25] and the HJC model [14, 26]. These models have been implemented and are available in commercial non-linear finite element solvers, such as ABAQUS [27] and LS-DYNA [28]. The K&C and RHT models are complex models, and require numerous material parameters not necessarily available in the design process. Thus, the models have been implemented with an automatic parameter generation option where the only required input parameter from the user is the unconfined compressive strength of the concrete. This omits the need for parameter identification, however, the calibration process becomes a black box for the user, where the accuracy of the parameters is uncertain [29, 30].

The HJC model allows for simpler material parameter calibration, but it does not include some characteristics known to be important for concrete, such as dependence on the third deviatoric stress invariant [31]. Polanco-Loria et al. [32] proposed three main modifications to the HJC model; the pressure-shear response of the original model was enhanced by including the influence of the third

deviatoric stress invariant to account for the difference in shear strength for the tensile and compressive meridians. Second, the strain rate sensitivity was altered such that the strain rate enhancement factor goes to unity for zero strain rate. Third, three damage variables were introduced to describe tensile cracking, shear cracking and pore compaction. The modified Holmquist-Johnson-Cook model (or MHJC) was coined a good compromise between simplicity and accuracy for large-scale computations of concrete plates impacted by projectiles. However, the modified model was only validated against a limited set of experimental data from the literature.

Recently, the MHJC model was validated against experimental data by Kristoffersen et al. [33]. Their work included an experimental study on 50 mm thick concrete slabs with different unconfined compressive strengths. Three sets of eight slabs were impacted by ogival steel projectiles with mass 0.196 kg. Parallel to the impact tests, the concrete strength was measured using standardised material tests, and the MHJC model was calibrated using results based on digital image correlation (DIC) [34] and a reverse-engineering approach using LS-OPT [35]. Subsequently, numerical studies were performed in LS-DYNA using a 2D axisymmetric model. The authors argued that the tensile strength exerted a significant influence on the ballistic limit velocities of the thin slabs.

As already stated, the MHJC model is considered a compromise between simplicity and accuracy, and is intended used in later studies involving large scale numerical simulations of concrete structures exposed to ballistic impact loading. In this study, the main objective is to further validate the rather simple and easily calibrated MHJC model in predicting the ballistic resistance of both plain and reinforced 100 mm thick concrete slabs impacted by ogival steel projectiles. To do so, the ballistic perforation resistance of a commercially produced concrete is investigated both experimentally and numerically, and the constitutive relation is calibrated using standardised material tests, 2D-DIC and some data from the literature. First, a number of 100 mm thick concrete slabs with nominal unconfined compressive strength of 75 MPa were cast. Two different reinforcement configurations with the same steel to concrete ratio were used to investigate a second objective, which is to assess the effect of reinforcement on the perforation resistance since the literature is somewhat inconsistent on this matter. Post curing, the concrete slabs were tested in the SIMLab gas gun facility [36] with ogival projectiles of mass 0.198 kg and diameter 20 mm, using initial velocities ranging from 235 m/s to 362 m/s. Synchronised high speed cameras were used to measure the velocities of the projectiles prior to and post impact, providing data for calculation of the ballistic limit velocity and curve for each reinforcement configuration. The calibrated constitutive relation was then used in

numerical simulations applying the non-linear finite element solver LS-DYNA. The accuracy and performance of a 2D axisymmetric and a 3D solid model were compared, and the results from both models were compared to the experimental data. Both the experiments and the numerical simulations suggest that the reinforcement affected the impact resistance of the concrete slabs through two main effects, namely confining and fragment trapping. Further, the numerical results indicate that the compressive strength of the concrete exerts a significant influence on the ballistic resistance for the 100 mm thick slabs tested in this study, in contrast to earlier results using rather thin target slabs with thickness 50 mm [33], where the compressive strength was found to be of secondary importance.

Materials

Casting and Fresh Concrete

In this study, only a concrete with a nominal compressive strength of 75 MPa was considered. Material tests of the fresh concrete were performed prior to casting. The fresh density, the air content, and the slump measure of the C75 concrete were found using standardised tests. The concrete was produced commercially, and the recipe from the manufacturer is listed in Table 1 along with the results from the material tests of the fresh concrete. During casting, the concrete was distributed and compacted in the forms using a steel rod. While it is possible to tailor the concrete recipe [37] to a larger extent than what is done herein, it is a notable point of this study to use a standard commercially available concrete for use in common concrete structures.

Cylinders and cubes were cast for material tests to calibrate the material parameters in the MHJC material model presented in Sect. "Numerical Simulations". 24 h post casting, the cubes and cylinders were demoulded, labelled, and weighed in both dry and submerged conditions. They were stored in a water container with a temperature of 20°C. The

Table 1 Concrete properties of the C75 concrete from manufacturer

Cement [kg/m ³]	434
Silica fume [kg/m ³]	49
Water [kg/m ³]	171
Fine aggregate 0-8 mm [kg/m ³]	917
Coarse aggregate 8-16 mm [kg/m ³]	873
MasterGlenium SKY899 [kg/m ³]	4.13
W/C-ratio [-]	0.394
Air content [%]	1.3
Slump [mm]	205
Density fresh concrete, ρ_{fresh} [kg/m ³]	2504

slabs were kept in the formwork and wrapped with a plastic cover. Anchor bolts were installed to provide lifting points.

A total of 24 slabs were cast with three different reinforcement configurations. Eight slabs were cast with an 8 mm hoop reinforcement around the perimeter for the sake of preventing secondary failure modes at the edges of the slabs post penetration. These slabs were unreinforced in the impact zone and labelled UA. The subsequent sixteen slabs were cast with two-layered grid reinforcement, eight with diameter 7 mm and spacing 150 mm, labelled A1, and eight with diameter 5 mm and spacing 75 mm, labelled A2. Both A1 and A2 give approximately the same reinforcement ratio $\rho_s = A_{\text{steel}}/A_{\text{concrete}}$. All reinforcement configurations are shown in Fig. 1. Like the concrete, the rebar steel was commercially produced. The reinforcement grids were placed with a centre-to-centre distance of 30 mm, thus leaving 35 mm of cover on each side, measured from the centre of the reinforcement cross-section. Furthermore, the grids were centred in the formwork and separated from the bottom of the forms using plastic spacers.

Material Tests

The concrete cubes had size 100 mm × 100 mm × 100 mm, and the cylinders had diameter 100 mm and height 200 mm. As concrete strength develops over time, it was important to perform material tests for the calibration at approximately the same time as the ballistic impact tests [33]. Cube compression tests, cylinder compression tests and tensile splitting tests were performed in parallel. In addition, material tests performed 28, 52 and 91 days post casting were instrumented with a camera synchronised to the force logger of the test machine to perform 2D-DIC. Specimens for cylinder compression were ground to have even and parallel surfaces. All material tests were performed in a Toni Technik 3000 [38] using a loading rate of 0.8 MPa/s. Figure 2 shows the development of the concrete strength over time, both

the cube compressive strength (a) and the tensile splitting strength (b). The dashed lines indicate the time interval in which the impact tests were conducted. [39] provides an expression for the strength development of concrete as

$$f(D_t) = \bar{f} \cdot \exp\left(s \cdot \left[1 - \left(\frac{\bar{D}}{D_t}\right)^{0.5}\right]\right) \quad (1)$$

The empirical parameters \bar{f} , s and \bar{D} were fitted to Equation (1) using a least squares fit and are listed in Table 2. The parameters were used to plot the curves in Fig. 2.

Table 3 provides the concrete density ρ_c , the cylinder compressive strength f_c , the cube compressive strength f_{cc} and the cylinder tensile splitting strength f_t , 28, 52 and 91 days post casting, respectively. All values are averages of the tests performed on their respective days.

From the strength development curves for the concrete, it can be seen that the cube strength had significant development until day 28 post casting, and further development to day 91. The tensile splitting strength seemed to have saturated at day 28, and no significant strength development occurred post 28 days. Both the cylinder compression strength and the cube compression strength were approximately 10 % higher on day 91 compared to day 28. The tensile splitting strength, however, was only 1.6 % higher on day 91 compared to day 28. From the literature, it is known that it is difficult to increase the tensile strength in proportion to compressive strength for high-strength concrete [40]. Thus, the resulting strength parameters of the concrete seem reasonable.

As stated, some of the material tests were synchronised with a camera to provide data for calibration of the MHJC material model. The specimens were coated with random speckles, and recorded during testing using a camera with image frequency 2 Hz. The images were synchronised with the force measurements from the Toni Technik test machine and recorded until specimen failure.

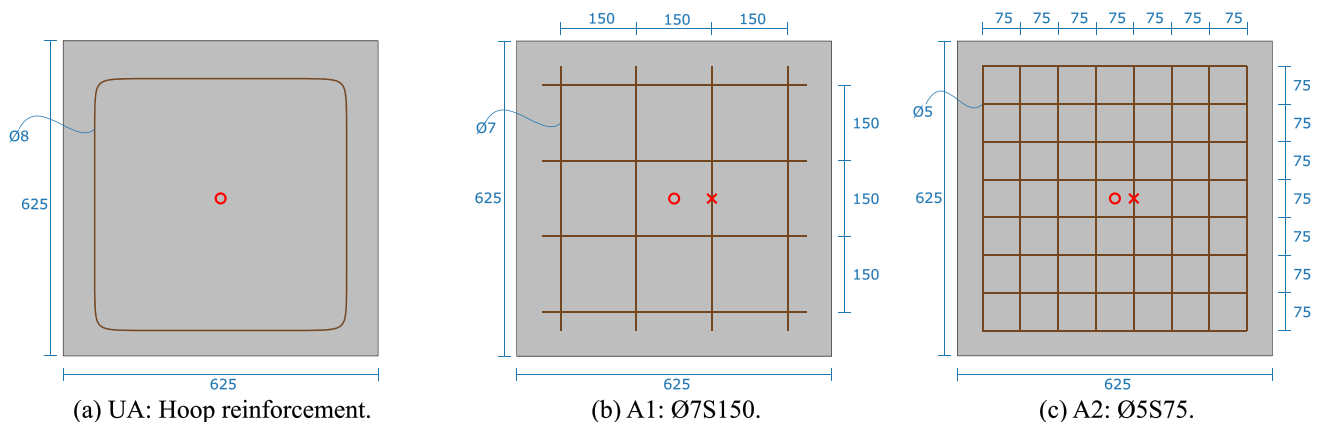


Fig. 1 Reinforcement grids. All measurements in mm. Most projectiles were aimed at the circles, while two projectiles were aimed at the crosses

Table 2 Strength development parameters, fitted to Equation (1)

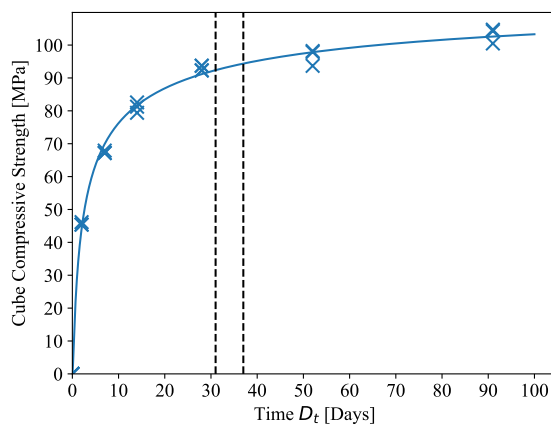
Test type	\bar{f} [MPa]	s [-]	\bar{D} [days]
Cube compression	94.5	0.229	37.5
Tensile splitting	5.8	0.158	36.3

Post-processing was performed using a subset analysis in the in-house DIC software eCorr [34]. In the 2D-DIC analyses, opposing subset pairs provided five estimates of the engineering strain. The axial engineering strain was found using $(l - l_0)/l_0$, where l is the current distance and l_0 is the initial distance in each subset pair.

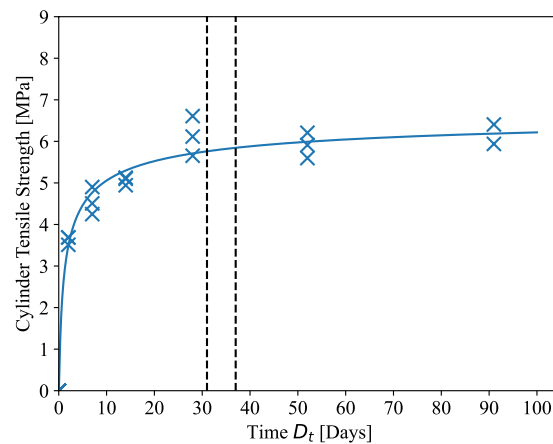
For the cylinder compression tests, the curved surface was used in the 2D-DIC analyses. As out of plane deformations were negligible, the same procedure with five subset pairs as for the cube tests was applied to track the axial strain in the specimens. The average of the measurements from the five subsets was used to represent each specimen. In the tensile splitting tests, subset pairs were placed to measure the transverse strain in each specimen. Figure 3 shows the placement of the subset pairs on (a) a cylinder compression specimen, (b) a cube specimen and (c) a tensile splitting (Brazilian) specimen. Figure 4 shows the engineering stress–strain curves for (a) the cylinder compression tests, (b) the cube compression tests and (c) the tensile splitting tests. All curves are averages of three tests performed 28 days post casting. Note that the data for the tensile splitting tests was filtered prior to plotting.

Figure 5 shows a typical effective strain field evolution as found by a 2D-DIC analysis in eCorr. The effective strain measure ϵ_{eff} is based on the von Mises norm [34], and is calculated as

$$\epsilon_{\text{eff}} = \sqrt{\frac{4}{3}(\epsilon_1^2 + \epsilon_1\epsilon_2 + \epsilon_2^2)} \quad (2)$$



(a)



(b)

Fig. 2 Concrete strength development over time. **a** Cube compressive strength f_{cc} . **b** Cylinder tensile strength f_t **Table 3** Development of concrete parameters

Days post casting	ρ_c [kg/m ³]	f_c [MPa]	f_{cc} [MPa]	f_t [MPa]
28	2484	82.7	93.0	6.1
52	2503	85.7	96.6	5.9
91	2516	91.6	103.2	6.2

where ϵ_1 and ϵ_2 are the in-plane principal logarithmic strains. The labels in Fig. 5 indicate the stress value. For the presented specimen, there is no visual damage on the surface in the left picture. In the middle picture, several cracks have developed, indicated by the red lines. The cracks continued to grow to complete failure, as seen in the right picture, taken post unloading. It appears that the 2D-DIC analysis captured the cracking in the specimen.

The data from the tensile splitting tests was filtered numerically due to some noise in the measurements. The noise is more pronounced in the tensile splitting tests because the strains are one order of magnitude lower compared with the compression tests. The engineering stress–strain curves for the cylinder compression tests will be used for calibration of the MHJC material model, which has proved successful in previous works [32, 33]. Engineering stress–strain curves from the cube compression tests will serve as validation of the calibrated material parameters.

In addition to material tests on the concrete, tensile tests were also performed on three steel specimens from each of the reinforcement diameters of 5 and 7 mm. The specimens were sharpened at the middle of the longitudinal direction to induce necking, and the initial diameters were measured with a micrometre. Tensile tests were performed in an Instron 5982 Tensile Machine [41], with a loading velocity of 3 mm/min. The deformation was recorded using a camera

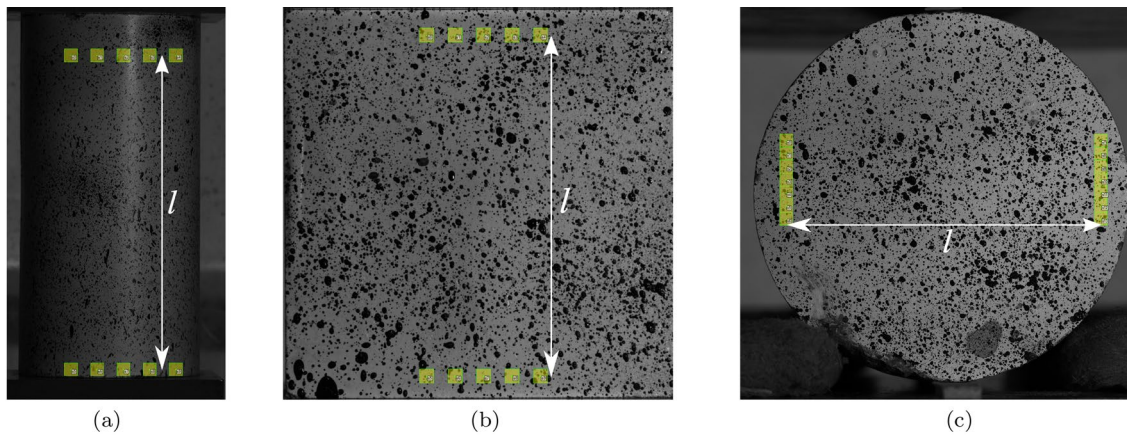


Fig. 3 Examples of subsets placement. **a** Subsets on cylinder. **b** Subsets on cube. **c** Subsets on cylinder

with a frequency of 2 Hz. The equivalent stress-plastic strain curves from these tests are shown in Fig. 6 a alongside the geometry of the specimens (b).

Component Tests

Experimental Setup

All ballistic impact tests were performed in a gas gun facility at NTNU as described by Børvik et al. [36]. The main components of the gas gun include a 200-bar pressure tank, a firing section, a 10 m³ impact chamber, a 10 m long 50 caliber barrel and a sabot trap. The projectile is placed in a 3D printed plastic sabot, and positioned into the barrel close to the firing section before it is accelerated towards the impact chamber. After two meters of free flight in the impact chamber, the sabot trap leaves the projectile free flying towards the target.

Ogival steel projectiles with diameter D_p of 20 mm and mass m_p of 0.198 kg were used in the impact tests. The caliber radius head (CRH) was 3, and the Rockwell C value

after heat treatment was measured to be 53. A picture of the projectile geometry is shown in Fig. 7.

The impact tests were performed 31 to 37 days post casting. The slabs were lifted out of the formwork and fastened in the impact chamber using clamps. All slabs and projectiles were weighed prior to and post impact. The reinforced slabs were scanned using a Proceq reinforcement scanner [42], and positioned such that the projectile would strike in the centre of the middlemost reinforcement grid. One slab from each reinforcement configuration was positioned such that the projectile struck the reinforcement. The plain slabs (UA) were positioned such that the projectiles impacted at the centre of the slabs.

Two synchronised Phantom v2511 high-speed cameras were used to record the impacts. Using DIC in post-processing, the camera setup allowed for measurements of the initial and residual velocities of the projectile, as well as the initial projectile pitch. The cameras were thus positioned to record the front and back of the slabs. The image frequency in these tests was 50 000 Hz, and lighting was provided by two Cordin 550 J flashlights and halogen lamps.

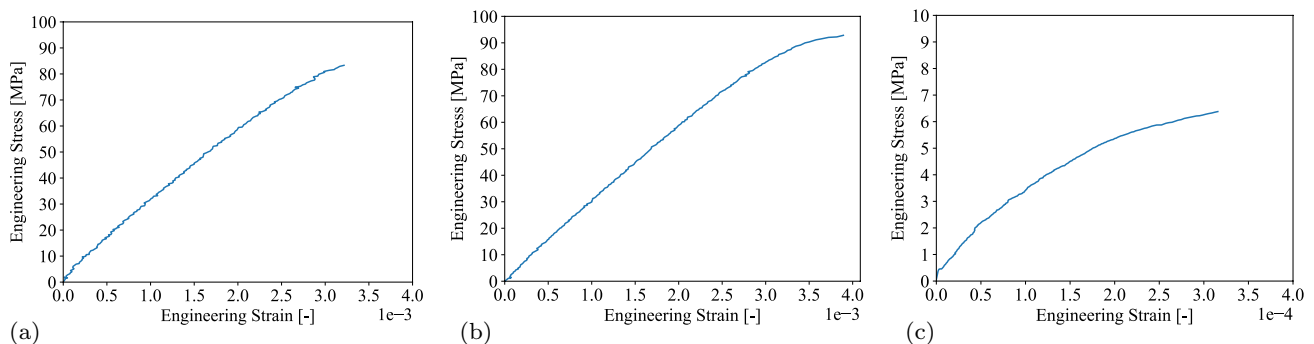


Fig. 4 Engineering stress–strain curves on day 28. Average of three tests. **a** Cylinder compression. **b** Cube compression. **c** Tensile splitting

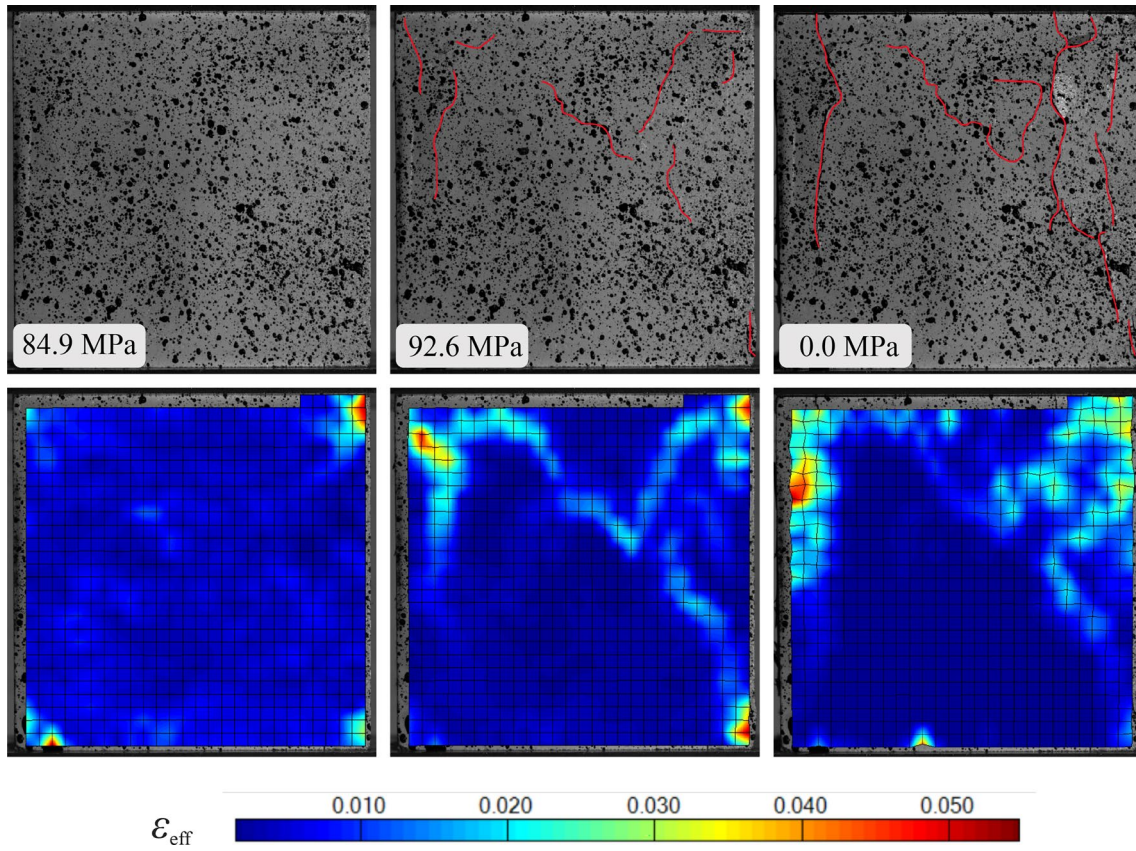
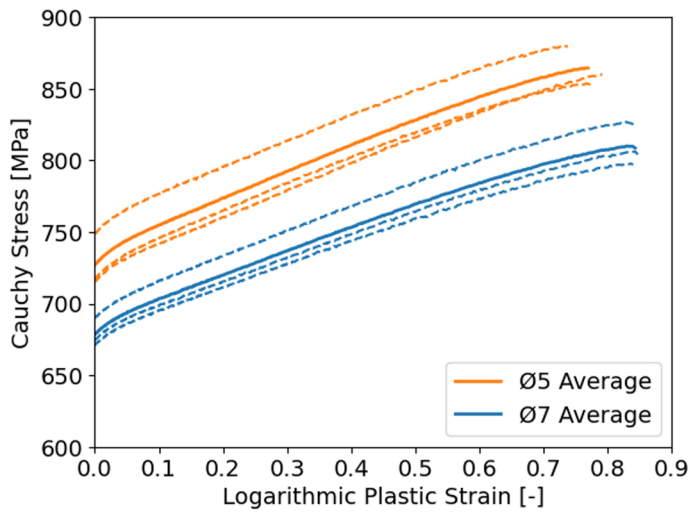
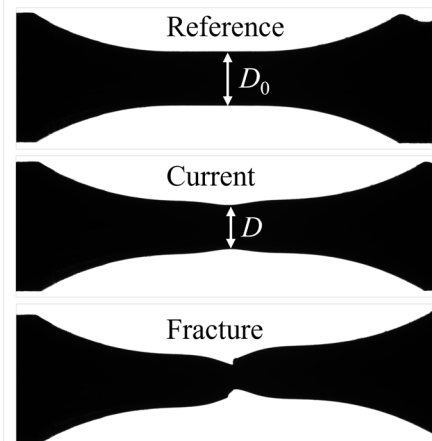


Fig. 5 Effective strain field on cube specimen. Stress value is stated for each image



(a) Cauchy stress-logarithmic plastic strain curves for rebar specimens. Solid line is average of dashed lines.



(b) Silhouettes of rebar specimens with diameter measurements.

Fig. 6 Results from steel tensile tests

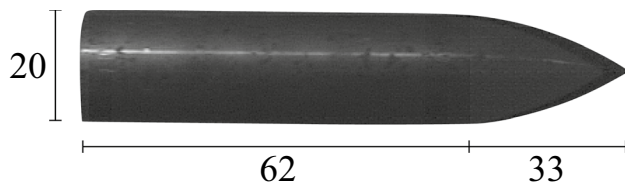


Fig. 7 Ogival steel projectile with dimensions in mm

Experimental Results

The main experimental results are presented in Table 4. The results include the slab thickness h_t , projectile pitch α , initial velocity v_i , residual velocity v_r , horizontal and vertical measurements of the spall d_{spall} and scab d_{scab} wounds, as well as initial mass m_i and final mass m_f of the slabs. The projectile masses are not reported in the table, as the maximum mass loss was found to be 0.4 %. The initial velocity measurements in the post-processing software were found to have a precision in the range ± 0.3 m/s, while the accuracy of the residual velocity measurements is less accurate due

to possible path changes and out-of-plane movements of the projectile after perforation.

The thicknesses of the slabs were measured using a caliper at eight different positions at the outer edge of the slabs. The thickness deviation was less than 1 % for all slabs. The maximum measured pitch α was 2.0° . While a sufficiently large impact angle may result in ricochets [43], experimental results reported by Goldsmith [44] showed that the penetration process is hardly affected by yaw angles up to $3\text{--}5^\circ$. Note that the total yaw $\gamma = \tan^{-1}(\tan^2\alpha + \tan^2\beta)^{1/2}$, where β is the yaw, has not been obtained, because the only measured angle was pitch. Furthermore, abrasions were observed on several projectiles post impact, but significant permanent deformation was not seen on any projectiles. Measurements of the spall and scab wounds were measured using a ruler in the horizontal and vertical direction. Figure 8 shows time-lapses from one test on each reinforcement configuration, with approximately the same initial velocity, close to the ballistic limit velocity. The fragments around the projectile in the first row of pictures are pieces from the shattered sabot. Note that all three projectiles were completely hidden in the slab for some time, and the large amount of dust

Table 4 Experimental results

Type	Slab #	h_t [mm]	α [°]	v_i [m/s]	v_r [m/s]	d_{spall} [mm]	d_{scab} [mm]	m_i [kg]	m_f [kg]	Δm [kg]
UA	3	100.4	0.5	235.5	0.0	200/200	360/280	97.4	94.8	2.6
UA [†]	4	99.9	2.0	244.7	0.0	180/180	410/280	96.8	92.6	4.2
UA	2	100.3	2.0	253.2	2.2	195/195	390/365	96.6	92.6	4.0
UA	7	99.7	0.5	265.4	2.6	165/185	385/425	97.3	92.6	4.7
UA [†]	6	100.3	1.0	276.6	0.0	240/200	360/360	96.9	92.7	4.2
UA	8	100.4	0.5	280.2	10.3	245/200	330/420	98.5	94.5	4.0
UA	1	100.2	0.5	301.9	62.5	165/190	260/245	97.2	95.6	1.6
UA	5	100.5	0.5	359.7	146.7	220/200	280/280	97.2	94.4	2.8
A1	4	100.4	0.5	252.7	0.0	210/215	230/220	98.2	96.1	2.1
A1	3	100.3	2.0	259.1	6.4	160/160	225/305	98.9	96.7	2.2
A1	7	100.4	0.0	274.0	36.0	120/125	260/290	98.8	95.8	3.0
A1 [†]	2	100.4	0.5	275.0	0.0	170/165	400/340	98.3	95.3	3.0
A1	6	100.3	0.5	296.7	49.0	240/225	310/340	98.8	95.0	3.8
A1*	1	100.4	1.0	299.6	11.8	200/200	340/380	98.2	93.7	4.5
A1	8	100.5	0.5	325.4	74.8	280/195	320/280	96.4	93.7	2.7
A1	5	100.4	0.0	361.1	180.1	195/170	340/280	97.1	93.8	3.3
A2	3	100.7	1.0	258.9	0.0	210/175	295/250	97.6	95.7	1.9
A2	7	100.3	0.5	260.9	21.0	205/185	265/235	97.7	95.3	2.4
A2	2	100.1	0.5	274.9	25.9	200/250	210/285	98.2	95.5	2.7
A2	1	100.5	0.5	292.3	21.8	210/215	290/340	98.7	95.5	3.2
A2	6	100.4	1.0	299.0	36.2	125/140	320/310	98.2	95.7	2.5
A2*	8	100.6	0.5	301.2	41.0	200/195	335/335	98.6	95.8	2.8
A2	5	100.2	1.5	327.3	80.8	160/175	270/280	97.7	94.7	3.0
A2	4	100.6	1.0	362.2	146.4	150/195	250/250	99.1	96.3	2.8

*Struck rebar

[†]Projectile completely obscured in video

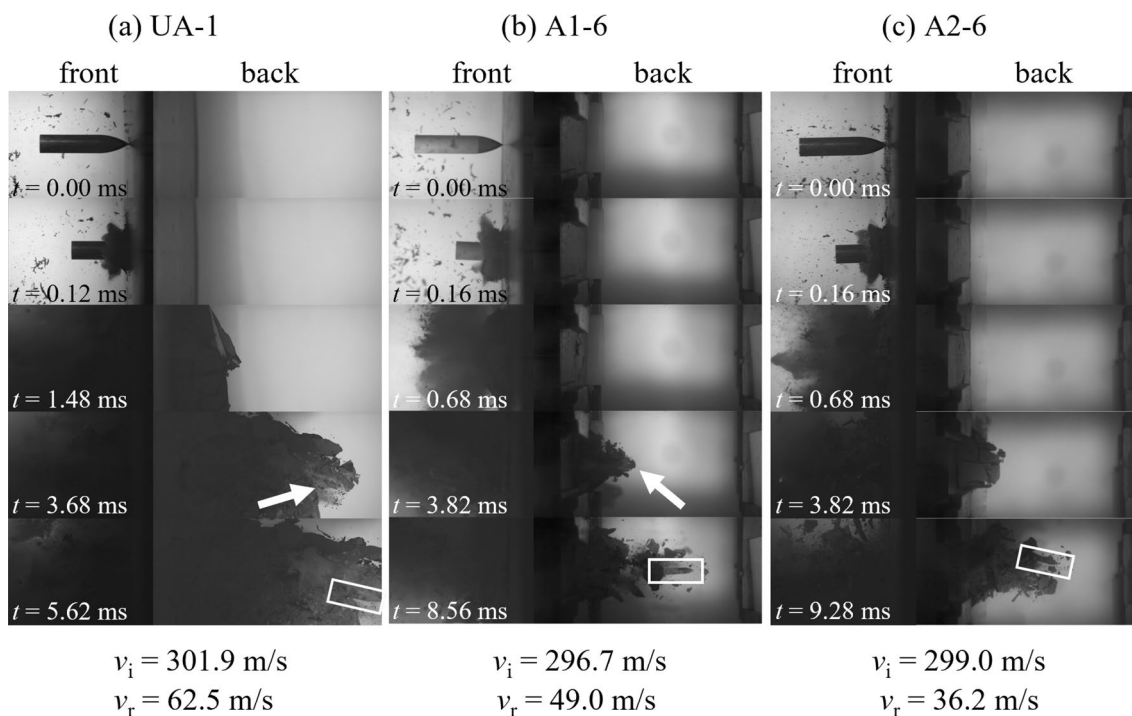


Fig. 8 Time-lapses for each configuration with $v_i \approx 300$ m/s

and fragments detaching from the slabs. In the pictures, the white arrows and boxes show the position of the projectile. Further, note that scabbing occurred for all tests, even when the projectiles did not perforate the slabs. For those tests, the projectiles punched holes in the slabs slightly smaller than the projectile diameter.

Experimental Observations

The average mass loss for the three slab sets was 3.5 kg, 3.1 kg and 2.7 kg, for slabs UA, A1 and A2, respectively. The scab craters were generally larger than the spall craters. Both the spall and scab measurements appeared lower for the reinforced slabs compared to the plain slabs, and decreased further when the spacing of the rebars was decreased. This is also supported by the average values for mass loss, as narrower spacing resulted in less ejected mass. Hence, reinforcement configuration A2, where the reinforcement had a closer grid, gave the least amount spalling and scabbing. However, the slabs that displayed minimum and maximum values for mass loss were both of type UA. Additionally, fragments detached from the backside of the slabs despite perforation not occurring. This is mostly due to the compression stress waves propagating through the slab thickness which are reflected as tension waves on the backside when a slab is impacted. For some of the reinforced slabs, fragments were hindered from detaching from the back of the slabs. This effect is called fragment trapping [9], and is exemplified

on slabs A2-1 (a) and A2-4 (b) in Fig. 9. The fragment trapping effect was most prominent for slabs of type A2. There seems to be no clear trend with respect to mass loss when varying the initial velocity.

The two experiments where the reinforcement was struck are indicated in Fig. 11. We observe that for the larger rebar diameter, there is a reduction in the residual velocity of the projectile compared to the test with almost the same initial velocity without striking any rebars. However, the same effect was not observed for the smaller rebar diameter. This indicates that the ballistic perforation resistance is affected by the rebar diameter when struck directly. However, it is not clear how much of this effect is caused by the scatter in the data, and it is thus difficult to draw any clear conclusion regarding the effect of striking the rebars based on the experiments in this study. This effect will be studied further in the numerical study.

Five slabs were sliced through the penetration channel to investigate the profiles of the craters. All five slabs had v_i of approximately 300 m/s. Figure 10 shows opposing cross-sections with the penetration channel outlined in red. The figure confirms that the scabbing crater is larger than the spalling crater. In concrete perforation tests, there is usually significant tunnelling between the two craters when the thickness is large enough [2, 45]. From Fig. 10, possible tunnelling effects are not clear. This indicates that the thickness is not large enough to clearly identify tunnelling. For two of the sliced slabs ((d) and (e)), the

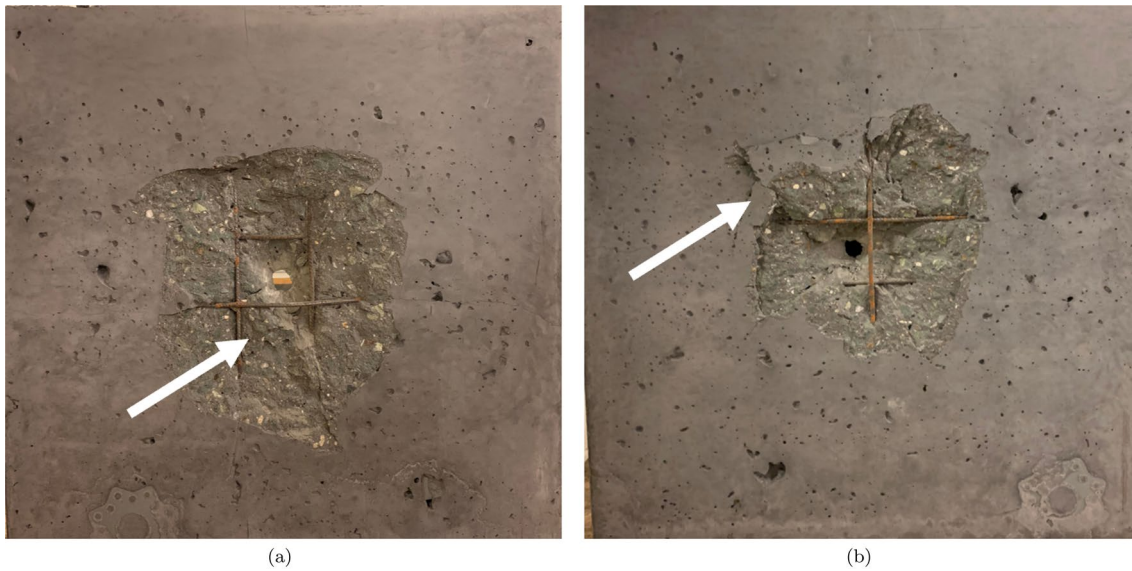


Fig. 9 Examples of fragment trapping. **a** Slab A2-1. **b** Slab A2-4

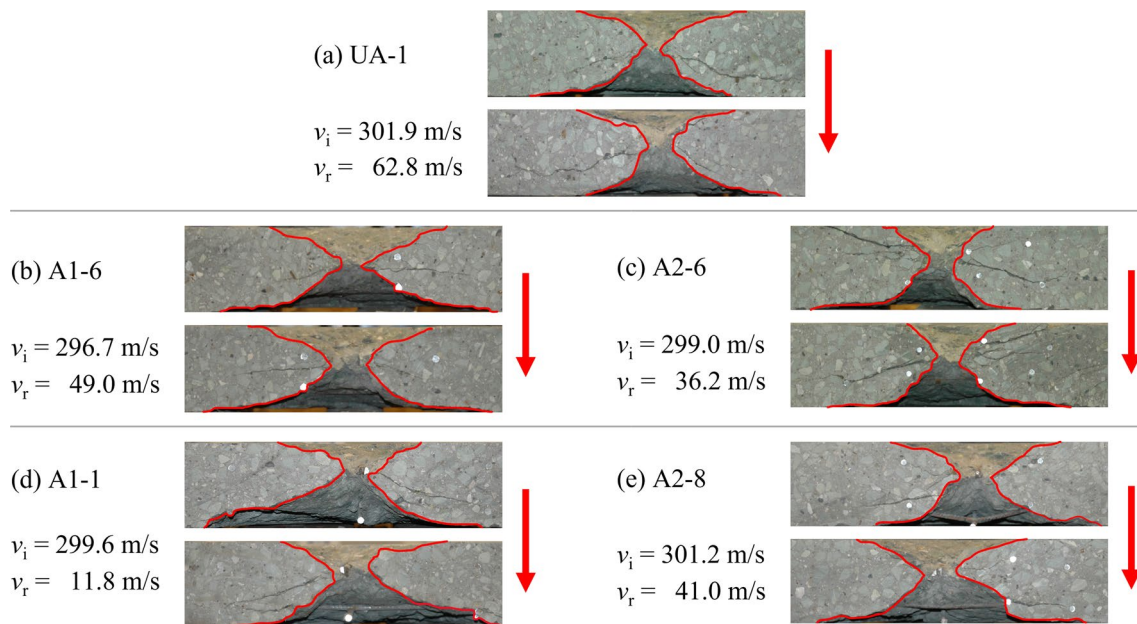


Fig. 10 Opposing cross-sectional slices of five slabs showing the perforation channel (red). The arrows indicate the impact direction (Color figure online)

projectiles struck the reinforcement. No clear difference regarding tunnelling was observed for these tests either, and it does seem like tunnelling effects are affected by adding reinforcement for the slabs in this study. Note that the front rebars were completely cut through, while the back rebars was severely bent. This is possibly due to trajectory deviation of the projectile during perforation.

Ballistic Limit Velocities and Curves

Ballistic limit velocities and curves can be found from the data presented in Table 4. The generalised Recht-Ipson model [46] was used with a least squares fit to calculate the model constants. Using conservation of momentum and

Table 5 Parameters fitted to the Recht-Ipson model

Reinforcement type	v_{bl} [m/s]	p [-]	a [-]
UA, No rebar	276.7	1.36	1.00
A1, Ø7S150	286.9	1.52	1.00
A2, Ø5S75	286.9	1.37	1.00

energy, the model defines the residual velocity after impact as

$$v_r = a(v_i^p - v_{bl}^p)^{1/p} \quad (3)$$

where a and p are model constants. It can be shown that $a = m_p / (m_p + m_{pl})$, where m_p is the mass of the projectile and m_{pl} is the mass of the plug and fragments. Theoretically, a should be close to unity and $p = 2$. However, in this study, a and p were considered empirical constants.

In some of the impact tests where the residual velocity was close to zero, perforation was considered to be driven by dynamic effects caused by the amount of debris that detached from the slab. These perforations were not considered clean perforations, and thus not used when calculating the model parameters in the Recht-Ipson model. The estimated model parameters for each slab type can be found in Table 5, and the corresponding ballistic limit curves are shown in Fig. 11. The parameter a was fixed to 1.00, and v_{bl} and p were fitted to the data points. For reinforcement configurations A1 and A2, the projectiles that struck reinforcement are indicated in the figures. Furthermore, a straight dashed line with a maximum slope of 1.0 has been drawn in each of the plots to indicate an area that contains all the tests with residual velocity larger than zero from the experiments performed in this study.

Determining the ballistic limit velocity exactly was difficult due to some scatter in the data. In some of the tests, the projectiles were completely obscured by fragments when exiting the slab. For these tests, that is UA-4, UA-6 and A1-2, the residual velocity was set to zero and excluded from the fit. When comparing the reinforced slabs to the plain slabs, adding reinforcement appeared to have minor effects on the ballistic limit velocity, increasing it by approximately 4 % for both series A-1 and A-2. Finally, the p -values for all slabs were found to be between 1.3 and 1.6.

Numerical Simulations

MHJC Material Model

The modified Holmquist-Johnson-Cook concrete model [32] was used for the numerical calculations. A description of the

main characteristics of the material model is presented in the following. In the MHJC model, the Cauchy stress tensor σ_{ij} is decomposed into deviatoric and hydrostatic parts

$$\sigma_{ij} = S_{ij} - P\delta_{ij} \quad (4)$$

where S_{ij} is the deviatoric part, $P = \sigma_{kk}/3$ is the hydrostatic pressure and δ_{ij} is the Kronecker delta. Furthermore, the von Mises equivalent stress is defined as

$$\sigma_{eq} = \sqrt{\frac{3}{2} S_{ij} S_{ij}} \quad (5)$$

The deviatoric part D'_{ij} of the rate of deformation tensor D_{ij} is defined by

$$D'_{ij} = D_{ij} - 1/3 D_{kk} \delta_{ij} \quad (6)$$

D'_{ij} is decomposed into an elastic and a plastic part by

$$D'_{ij} = D'^{e}_{ij} + D'^{p}_{ij} \quad (7)$$

where

$$D'^{e}_{ij} = \frac{1}{2G} S_{ij}^{\nabla J}, \quad D'^{p}_{ij} = \dot{\epsilon}_{eq}^p \frac{3}{2} \frac{S_{ij}}{\sigma_{eq}} \quad (8)$$

In this expression, $S_{ij}^{\nabla J}$ is the Jaumann rate of the stress deviator, G is the shear modulus and $\dot{\epsilon}_{eq}^p$ is the equivalent plastic strain rate, given by

$$\dot{\epsilon}_{eq}^p = \sqrt{\frac{2}{3} D'^{p}_{ij} D'^{p}_{ij}} \quad (9)$$

To avoid a discontinuous description for $P^* = 0$, the modified model presents the normalised equivalent stress as

$$\sigma_{eq}^* = \frac{\sigma_{eq}}{f_c} = \begin{cases} B[P^* + T^*(1-D)]^N F(\dot{\epsilon}_{eq}^*) R(\theta, e) \leq S_{max} & \text{for } P^* \geq -T^*(1-D) \\ 0 & \text{for } P^* < -T^*(1-D) \end{cases} \quad (10)$$

where $T^* = T/f_c$ and T is the maximum tensile hydrostatic pressure the material can withstand, assumed equal to f_t as recommended by Polanco-Loria et al. [32]. The function $F(\dot{\epsilon}_{eq}^*)$ is a function of the normalised equivalent strain rate and accounts for the strain rate sensitivity of the material. It is defined as

$$F(\dot{\epsilon}_{eq}^*) = [1 + \epsilon_{eq}^*]^C \quad (11)$$

where C is the strain rate sensitivity parameter. $R(\theta, e)$ is a function of the deviatoric angle θ and the normalised out-of-roundness parameter e , stated as

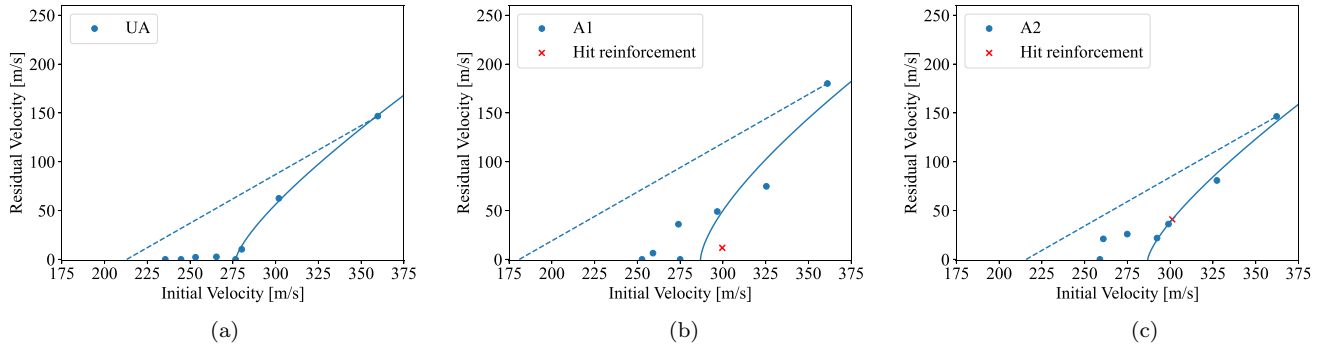


Fig. 11 Resulting experimental ballistic limit curves. **a** UA, No reinforcement. **b** A1, Ø7S150. **c** A2, Ø5S75

$$R(\theta, e) = \frac{2(1 - e^2)\cos\theta + (2e - 1)[4(1 - e^2)\cos^2\theta + 5e^2 - 4e]^{1/2}}{4(1 - e^2)\cos^2\theta + (1 - 2e)^2} \quad (12)$$

This function was introduced in the MHJC model to account for the reduction of shear strength on the compressive meridian. Furthermore, the model accounts for the pressure sensitivity of concrete by separating the pressure-volume response into three different regions. The first region is linear elastic, and limited by $(\mu_{\text{crush}}, P_{\text{crush}})$, where P_{crush} is the pressure that occurs in a uniaxial compression test and μ_{crush} is the corresponding volumetric strain. The second region is a transition region, limited by $P_{\text{crush}} \leq P \leq P_{\text{lock}}$, where P_{lock} is the pressure where all air voids are removed from the concrete and μ_{lock} is the corresponding strain. In this region, the air voids are gradually compressed out of the concrete, resulting in volumetric plastic strains. The third region starts when all air voids are removed from the concrete, resulting in a fully dense material. Then, the pressure is expressed as a function of the modified volumetric strain $\bar{\mu}$, as $P = K_1\bar{\mu} + K_2\bar{\mu}^2 + K_3\bar{\mu}^3$, while $\bar{\mu}$ is defined as

$$\bar{\mu} = \frac{\mu - \mu_{\text{lock}}}{1 + \mu_{\text{lock}}} \quad (13)$$

The parameter K_1 is dependent on the shear modulus G , and can be expressed as

$$K_1 = \frac{2(1 + \nu)}{3(1 - 2\nu)}G \quad (14)$$

The total damage D in the model is calculated as

$$(1 - D) = \sqrt{(1 - D_S)(1 - D_C)} \quad (15)$$

where D_S is the shear damage, and D_C is the compaction damage. The damage evolution is described by

$$\dot{D}_S = \frac{\dot{\epsilon}_{\text{eq}}^p}{\epsilon_f^p}, \dot{D}_C = \frac{\dot{\mu}^p}{\mu_{\text{lock}}} \quad (16)$$

where the plastic strain to fracture is found from

$$\epsilon_f^p = \alpha(P^* + T^*)^\beta \geq (\epsilon_f^p)_{\text{min}} \quad (17)$$

where α and β are fracture parameters. $\dot{\mu}^p$ is the plastic volumetric strain rate. The MHJC material model is implemented in the explicit non-linear FEM solver LS-DYNA R12 as a user defined material model (UMAT). The reader is referred to [32] for a complete description of the model.

Model Calibration

To calibrate the material parameters not found directly from material tests nor in the literature, an inverse numerical modelling approach in LS-OPT [35] was used. LS-OPT is a graphical optimisation tool that interfaces with LS-DYNA, well suited for material calibration, and was used to calibrate the fracture constants α and β , the pressure hardening exponent N and the pressure hardening coefficient B in the MHJC model, as well as the shear modulus G .

A 2D axisymmetric numerical model of the cylinder compression test was created with dimensions 200 mm × 50 mm, representing a cylinder with height 200 mm and diameter 100 mm after rotating about the symmetry axis. The cylinder was compressed by two rigid steel platens, one fixed and one moving in the loading direction. Typical steel parameters were assigned to the platens, with the density set to 7800 kg/m³, Young's modulus of 210 GPa and Poisson's ratio of 0.33. Contact was modelled using a 2D automatic surface-to-surface formulation, with a frictional coefficient of 0.37. Baltay and Gjelsvik [47] presented values for the static and dynamic frictional coefficients of steel in the range 0.2 to 0.6, but as reported by Kristoffersen et al. [33], varying the frictional coefficient in this type of test did not affect the results significantly. The cylinder was assigned the MHJC model as a UMAT. The model geometry (a) and a comparison of the resulting engineering stress–strain curve to the experimental curve (b) are presented in Fig. 12, where the nodes used to measure the engineering strain are indicated by yellow dots in (a).

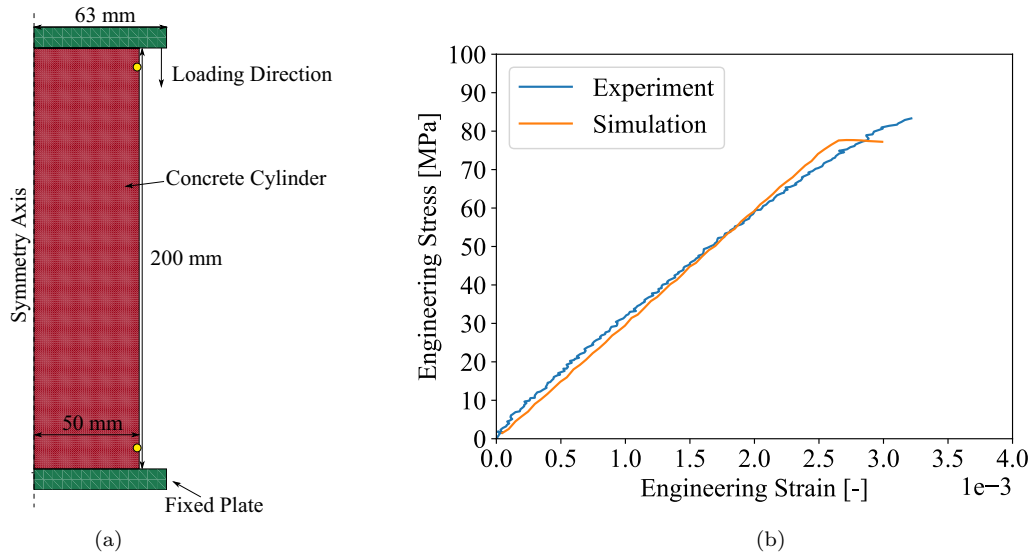


Fig. 12 Axisymmetric model of concrete cylinder. **a** Geometry of LS-OPT model. **b** Comparison with experiment

In the actual experiments, the duration of the cylinder compression tests was approximately 100 s. To avoid extensive simulation time in the numerical model, a time scaling factor of 10^4 was used, resulting in a simulated time for the analysis of 0.01 s. Due to the time scaling, the strain rate sensitivity constant C was set to zero. As the actual tests had a loading rate of 0.8 MPa/s, they were considered quasi-static [48] and strain rate effects were neglected. However, C was still needed for the impact tests and set to 0.04 in the ballistic impact simulations based on Polanco-Loria et al. [32]. The resulting material parameters from the optimisation are presented in Table 6.

Verification with Cube Model

To assess the validity of the calibrated material parameters, a cube compression test was simulated. A 3D model of a cube specimen was created in LS-DYNA with two symmetry planes. The model consisted of three parts, namely the bottom platen, the top platen, and the cube specimen. The element size was $1 \text{ mm} \times 1 \text{ mm} \times 1 \text{ mm}$, and constant stress solid elements (element formulation 1 in LS-DYNA) were used. Contact was modelled using an automatic node-to-surface formulation, with a frictional coefficient of 0.37. As with the cylinder compression simulations, the strain rate sensitivity parameter C was set to zero. The total number of elements in the numerical model was $2.5 \cdot 10^5$. A comparison of the stress–strain curves from the cube experiments and the numerical simulation can be seen in Fig. 13.

Table 6 Material parameters MHJC model

Parameter	Unit	From	Value
ρ_c	[kg/m ³]	Tests	2522
f_c	[MPa]	Tests	82.7
f_{cc}	[MPa]	Tests	93.0
f_i	[MPa]	Tests	6.1
$\dot{\epsilon}_0$	[1/s]	Tests	10^{-5}
P_{crush}	[MPa]	$\frac{f_c}{3}$	27.6
μ_{crush}	[-]	$\frac{f_c}{3K_1}$	$1.66 \cdot 10^{-4}$
K_1	[MPa]	Equation (14)	16566.8
G	[MPa]	LS-OPT	12425.1
B	[-]	LS-OPT	1.356
N	[-]	LS-OPT	0.368
α	[-]	LS-OPT	0.124
β	[-]	LS-OPT	1.681
ν	[-]	Literature	0.20
K_2	[MPa]	Literature	-171000
K_3	[MPa]	Literature	208000
$(\epsilon_f^p)_{min}$	[-]	Literature	0.002
P_{lock}	[MPa]	Literature	800
μ_{lock}	[-]	Literature	0.01
C	[-]	Literature	0.04
S_{max}	[-]	Literature	7.0

The force in the numerical model was found using a cross-section plane perpendicular to the loading direction. The strain was found from the distance between two nodes, in the same manner as for the subsets in the experiments. As

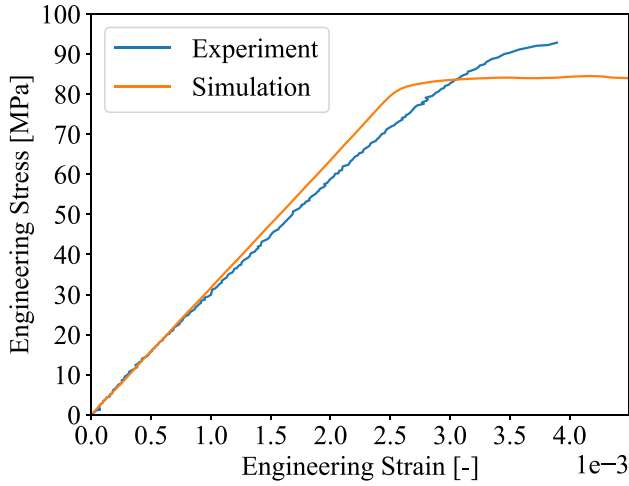


Fig. 13 Validation of MHJC parameters using a 3D cube model

seen in Fig. 13, the agreement between the test and simulation was acceptable.

Calibrating the Steel Parameters

To calibrate the material parameters of the steel reinforcement, 2D edge tracing in eCorr was used for post-processing of the data from the tensile tests to track the diameter reduction. The strain in each specimen was found using

$$\epsilon_1 = \ln\left(\frac{A_0}{A}\right) = 2\ln\left(\frac{D_0}{D}\right) \quad (18)$$

where A_0 is the initial area in the specimen prior to testing calculated from the initial diameter D_0 . A is the current area calculated from the current diameter D measured by edge tracing. Three tests from each diameter were averaged to calibrate the material parameters for the modified Johnson-Cook material model [49]. Therein, the equivalent stress σ_{eq} is a function of the yield strength, strain hardening, strain rate hardening and temperature softening, viz.

$$\sigma_{eq} = \left(A + \sum_{i=1}^2 Q_i(1 - e^{-C_i p})\right)(1 + \dot{p}^*)^C(1 - T^{*m}), \quad (19)$$

where A , C , m , Q_1 , C_1 , Q_2 and C_2 are model parameters. $\dot{p}^* = \dot{p}/\dot{p}_0$ is the normalised plastic strain rate, where \dot{p}_0 is a user-defined reference strain rate. The homologous

temperature is defined as $T^* = (T - T_r)/(T_m - T_r)$, where T is the absolute temperature, T_r is the room temperature and T_m is the melting temperature. The data for the Cauchy stress and logarithmic plastic strain was fitted to Equation (19), and is plotted in Fig. 6 a. To model fracture in the reinforcement, the Cockcroft-Latham fracture criterion [50] was used. W_c limits the plastic work per volume, and erodes an element when the critical value is reached. W_c was found by calculating the area under the Cauchy stress-logarithmic plastic strain curve until failure. The resulting model parameters can be found in Table 7. Additionally, the density was set to 7800 kg/m^3 , Young's modulus 210 GPa , Poisson's ratio 0.33 , and a specific heat value C_p of 452 J/kgK was used.

2D Modelling of Plain Slabs

The 2D axisymmetric model of the ballistic impact test was established in LS-DYNA, and consisted of a rectangular 2D slab and a projectile. Both parts were modelled with an element size of $1 \text{ mm} \times 1 \text{ mm}$. By utilising the same element size as in the material calibration, a computational cell approach was ensured [51], thereby reducing mesh sensitivity in the model. The experimental setup in the gas gun only exposed a circular part with diameter 520 mm for the slabs, and the slab was thus modelled as a rectangle with dimensions $260 \text{ mm} \times 100 \text{ mm}$, resulting in a circular slab when rotating about the symmetry axis. The average slab thickness in the experiments varied with less than 1 % from the nominal thickness of 100 mm , and the thickness in the numerical simulations was therefore set to the nominal value. The total number of elements in the slab was $2.6 \cdot 10^4$.

Axisymmetric volume weighted shell elements (element formulation 15 in LS-DYNA) were used for both parts. The projectile was modelled as a rigid part with density 7800 kg/m^3 , Young's modulus 210 GPa and a Poisson's ratio of 0.33 . A pinhole with diameter 0.1 mm was applied to avoid strong distortion of the elements under the tip of projectile. The total amount of elements in the projectile was 840 . The model prior to impact can be seen in Fig. 14a.

Furthermore, the slab was assigned the calibrated MHJC material model through a UMAT, with parameters as presented in Table 6. To ensure erosion of elements with high strains, erosion criteria with the maximum effective strain (EFFEPS) and the maximum principle strain (MXEPS), both equal to 1.0 , were included using MAT_ADD_EROSION. Contact between the two parts was modelled as an automatic single surface 2D

Table 7 Material parameters for reinforcement steel

Diameters [mm]	A [MPa]	Q_1 [MPa]	C_1 [-]	Q_2 [MPa]	C_2 [-]	ϵ_0 [s^{-1}]	C [-]	m [-]	W_c [MPa]
7	682.3	130.8	0.66	177.1	0.66	$5 \cdot 10^4$	0.010	1.0	620
5	731.6	135.8	0.68	199.5	0.68	$5 \cdot 10^4$	0.010	1.0	620

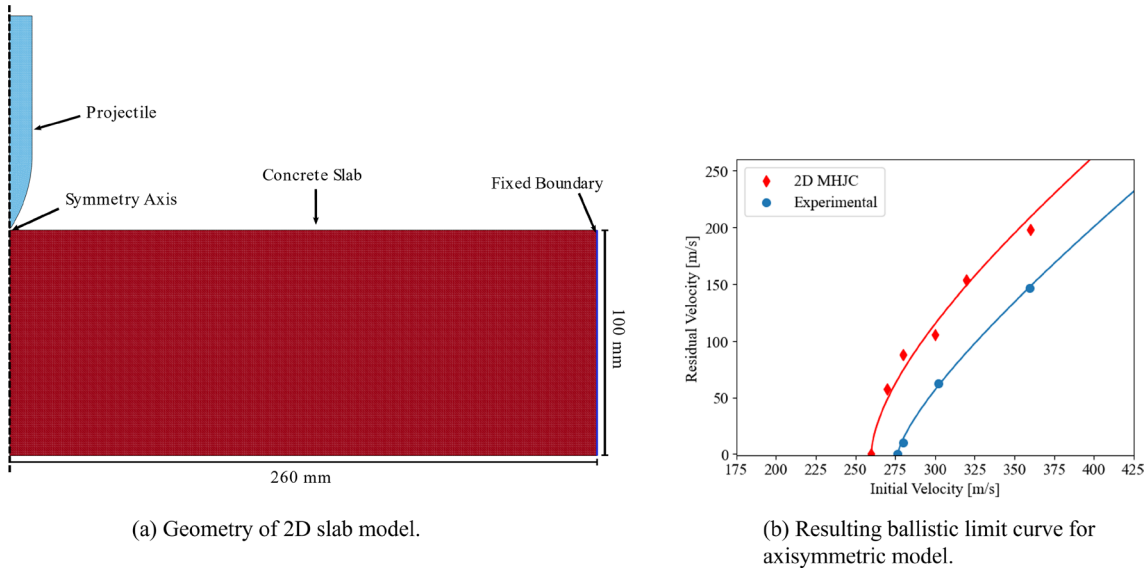


Fig. 14 Axisymmetric model

contact type, with the scale factor for penalty force stiffness set to 3.0. Friction was set to zero as a conservative estimate. The projectile nodes along the symmetry axis were restricted to move merely in the impact direction. The nodes on the right boundary of the slab were fixed.

Analyses were run with initial velocities ranging from 260-360 m/s, and the simulated times were 1-3 ms. The data points were fitted to the Recht-Ipson model, and the resulting plot is compared to the experimental data in Fig. 14b. The ballistic parameters are summarised in Table 8. The axisymmetric model underestimated the ballistic limit velocity for the slab by 6 %, with simulation times of 2-3 min when run in parallel on 16 CPUs on a high-performance cluster, making it suitable for a parameter study.

The strength parameters are among the most descriptive and quantifiable parameters when investigating the concrete behaviour. In the parameter study, one of the parameters f_c and f_t was altered at a time, either halved or doubled. The material model was updated with the material parameters and the impact simulations were re-run. Halving the unconfined compressive strength from 82.7 MPa to 41.4 MPa resulted in a 19.2 % decrease in ballistic limit velocity, while doubling f_c to 165.4 MPa increased the ballistic limit velocity by 19.2 %.

Varying the tensile strength also affected the ballistic resistance. Halving f_t from 6.1 MPa to 3.1 MPa resulted in an 11.5 % decrease in ballistic limit velocity, while doubling f_t resulted in an increase of 5.8 %. It thus seems that the unconfined compressive strength had considerably larger

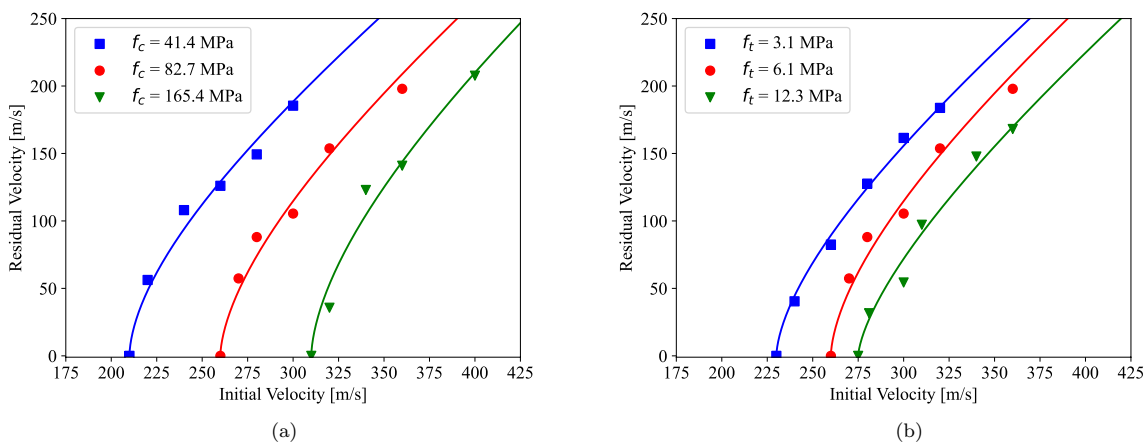


Fig. 15 Ballistic limit curves for parameter study on strength. a Cube compressive strength f_{cc} . b Cylinder tensile strength f_t

effect on the ballistic resistance compared to the tensile strength. This suggests that v_{bl} depends strongly on f_c for the 100 mm thick slabs, which is different to the findings of [33] for 50 mm thick slabs. The resulting ballistic limit curves for f_c (a) and f_t (b) are compared to the reference model in Fig. 15.

For dynamic problems, the effects of strain rate are important [49]. The specific strain rate sensitivity of the C75 concrete used in this study is not known. However, previous studies [32, 33] have used a strain rate parameter C equal to 0.04 for concretes with similar strengths. To study the effects of strain rate, two new series of simulations were run, using C -values of 0.00 and 0.08. Completely omitting the strain rate resulted in a reduction of v_{bl} of 30.7 %. Doubling C increased v_{bl} by 23.1 %. It thus seems both safe and reasonable to include strain rate effects, however, notice that the effect of increasing C is significant. Further, it is generally difficult to discern strain rate effects from inertial effects in material tests [52]. We also note that concrete has different strain rate sensitivity in compression and tension [53], however, the study of these differences are considered to be out of scope for this study. The resulting ballistic limit curves from the parameter study can be seen in Fig. 16a.

In the reference model, μ was conservatively set to zero. To study frictional effects, μ was set to 0.40 and assumed equal for both static and dynamic friction. Including frictional effects increased v_{bl} by 24.4 %. In a ballistic impact problem, the projectile must push material away from its trajectory to allow for penetration and perforation. This process dissipates energy when $\mu > 0$, and it is thus reasonable that increasing μ increases the ballistic resistance of the model. The resulting curves can be seen in Fig. 16b.

Finally, the effect of varying the Poisson's ratio ν of the concrete was studied. In the reference model, ν was set to 0.20. In the parameter study, decreasing ν to 0.10 resulted in an increase in v_{bl} of 3.8 %, while increasing ν to 0.30 decreased v_{bl} by 3.8 %. It thus seems that varying ν had a minor effect on v_{bl} for the 100 mm thick slabs. The resulting

curves can be seen in Fig. 16c. The results from the parameter study are summarised in Table 8.

3D modelling of Plain Slabs

In addition to the axisymmetric 2D model, a full 3D model with solid elements was created in LS-DYNA to model the component tests. The slab was modelled with dimensions 520 mm \times 520 mm \times 100 mm with no symmetry planes, and meshed in different zones, as shown in Fig. 17. Note that the projectile nose is truncated to avoid strong distortion of elements under the tip of the projectile. The total number of elements in the slab was $3.02 \cdot 10^6$, with element size 1 mm \times 1 mm \times 1 mm in the impact zone. Constant stress solid elements (element formulation 1 in LS-DYNA) were used for both the slab and the projectile. The projectile was modelled as a rigid part with dimensions from Fig. 7. Material model and parameters for the slab and the projectile were equal to those in the 2D axisymmetric model. Interior contact was included in the slab, and contact between the projectile and the slab was modelled with an eroding surface-to-surface formulation. The scale factor for the penalty stiffness was set to 1.5. The nodes on the outer edge of the slab were fixed.

Table 8 Recht-Ipson model parameters for the parameter study compared to reference model

Parameter	Value	v_{bl} [m/s]	p [-]	a [-]	Deviation [%]
Reference	–	260.0	1.64	1.00	–
f_c	41.4 MPa	210.0	1.70	1.00	–19.2
f_c	165.4 MPa	310.0	1.65	1.00	19.2
f_t	3.1 MPa	230.0	1.61	1.00	–11.5
f_t	12.3 MPa	275.0	1.48	1.00	5.8
C	0.00	180.3	1.47	1.00	–30.7
C	0.08	320.0	1.83	1.00	23.1
μ	0.40	323.6	1.38	1.00	24.4
ν	0.10	270.0	1.65	1.00	3.8
ν	0.30	250.0	1.60	1.00	–3.8

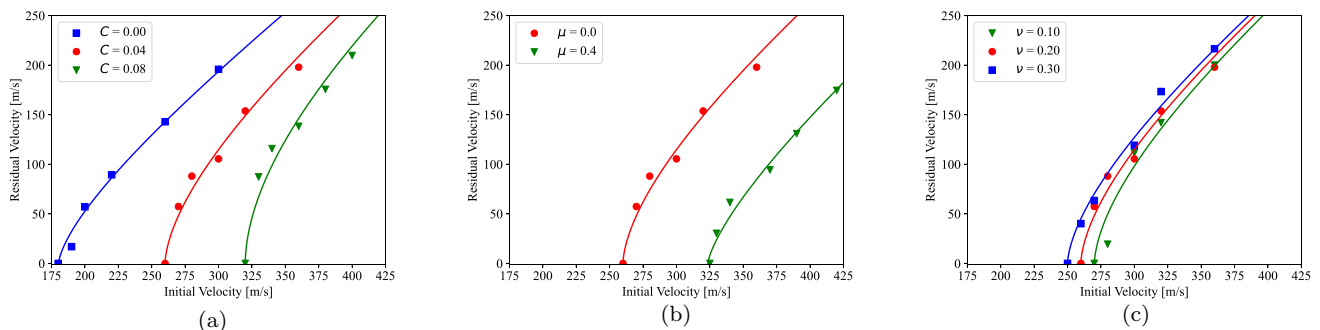
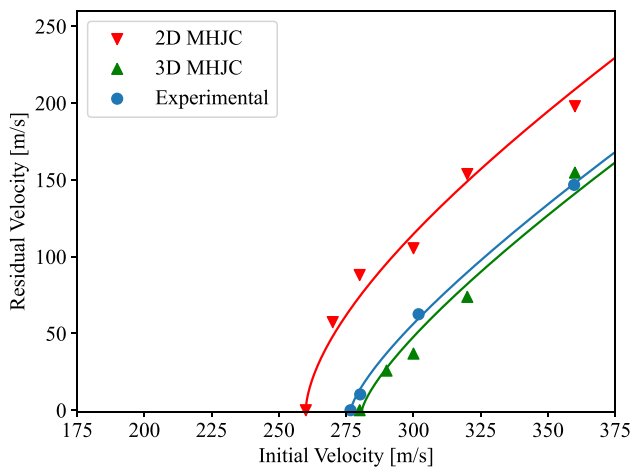
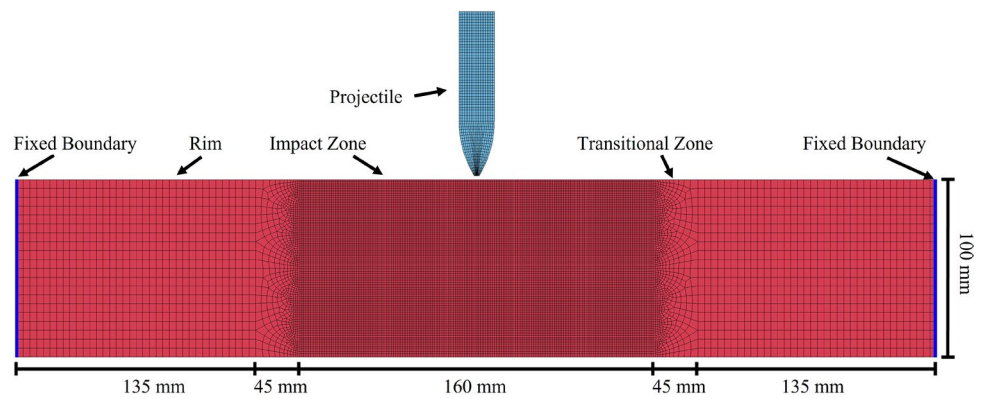


Fig. 16 Ballistic limit curves for parameter study on C , μ , and ν . **a** Strain rate sensitivity C . **b** Friction coefficient μ . **c** Poisson's ratio ν

Fig. 17 Cross-section of 3D slab model geometry**Fig. 18** Comparison of ballistic limit curves for the 2D model, 3D model and the experiments**Table 9** Comparison of the calibrated Recht-Ipson model parameters for plain slabs

Model	v_{bl} [m/s]	p [-]	a [-]
Experimental	276.7	1.36	1.00
2D Axisymmetric	260.0	1.64	1.00
3D Solid	280.9	1.34	1.00

The projectile was assigned initial velocities in the impact direction. The resulting data for initial velocities in the range 260–360 m/s are shown in Fig. 18, with the resulting Recht-Ipson fit. The resulting ballistic parameters are compared to the experimental values and the results from the 2D axisymmetric model in Table 9. The 3D model overestimated the ballistic limit velocity by 1%. However, the residual velocities were overestimated for velocities above v_{bl} , yielding conservative results. The simulation times for the 3D model were between 10 and

29 h on a high-performance cluster using 16 CPUs. Thus, the CPU time increased by a factor 300–600 compared to the axisymmetric model.

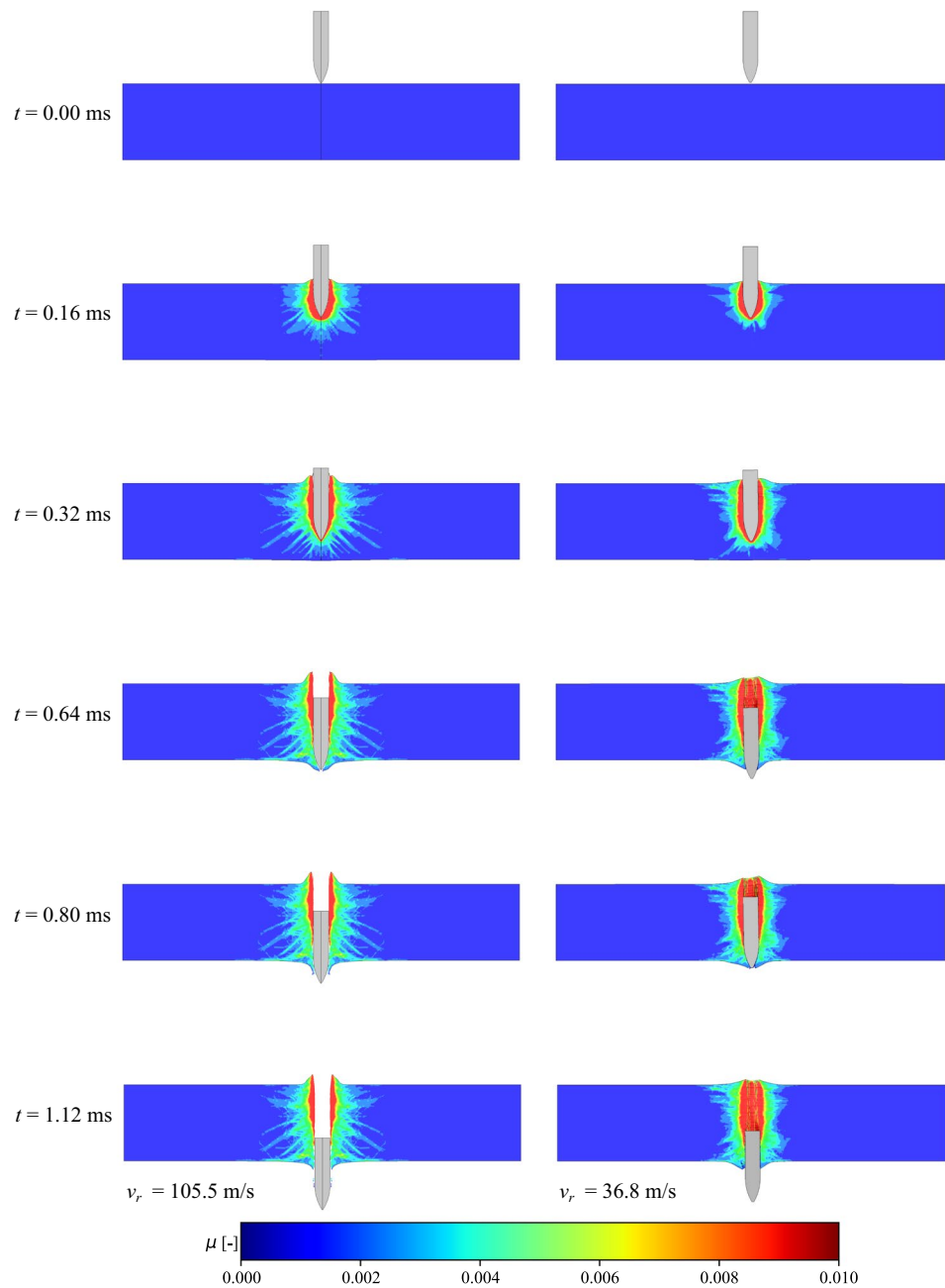
Figure 19 shows a comparison of the volumetric strain evolution during penetration for a 2D simulation and a 3D simulation with $v_i = 300$ m/s. Generally, the shape of the resulting strain pattern is similar to the perforation channels from the experiments shown in Fig. 10. However, the scabbing cones are smaller than that of the experiments and there is almost no fragmentation. Also, the volumetric strain does not differ significantly between the two models.

Element erosion is a technique commonly used for FE simulations, and can be introduced in LS-DYNA by using the MAT_ADD_EROSION keyword. To highlight the effect of different values of the erosion criteria, we performed a series of simulations on the 3D model. As stated, the 2D model and the reference 3D model employed values for the maximum effective strain (EFFEPS) and maximum principle strain (MXEPS) of 1.0. To study the effect on ballistic perforation resistance in the 3D model, values for both criteria of 0.5 were used. Figure 20 shows the resulting ballistic limit curve compared to the reference model.

3D modelling of Reinforced Slabs

In the component tests, we observed that adding reinforcement to the concrete slabs had negligible effect on the ballistic resistance when not striking the reinforcement. However, a reduction in residual velocity was seen for A1 compared to UA and A2 for the same initial velocity when the projectile struck the reinforcement. To study the effect of reinforcement in the slabs numerically, a reinforcement mesh was embedded in the aforementioned solid slab mesh. Simulations where projectiles did not strike the reinforcement yielded exactly the same ballistic parameters as the plain slab simulations, and are thus not presented in detail in this study. Direct interaction between projectile and rebars was also simulated. To avoid extensive simulation times, the reinforcement was only added in the impact zone of the

Fig. 19 Volumetric strain for 2D model (left) and 3D model (right) with $v_i = 300$ m/s. Slab UA-1 from experiments: $v_i = 301.9$ m/s and $v_r = 62.5$ m/s



slab. Preliminary studies showed no significant strains in the reinforcement outside the impact zone. Interaction between the reinforcement grid and the slab was modelled using a solid-in-solid contact, thus assuming a perfect bond. Contact with the projectile was modelled using a surface-to-surface formulation. Reinforcement diameters from 5 to 8 mm were investigated. All meshes had element size of approximately 1 mm, and constant stress solid elements (element formulation 1 in LS-DYNA) were used.

The reinforcement was modelled using the modified Johnson-Cook material model [54], that is MAT_107 in

LS-DYNA, with the calibrated material parameters for A1 from Table 7. Simulations were run with an initial velocity of 300 m/s. Simulation times were between 46 and 110 h with the same computational power as the simulations of the plain slabs. Table 10 shows the numerical results for all reinforcement diameters. In all simulations, the projectile struck both layers of reinforcement. It is interesting to see that for the smallest simulated rebar diameter, the projectile perforated the slab with a higher residual velocity than the plain slab. Fringe plots of the volumetric strain in the concrete during penetration is shown in Fig. 21.

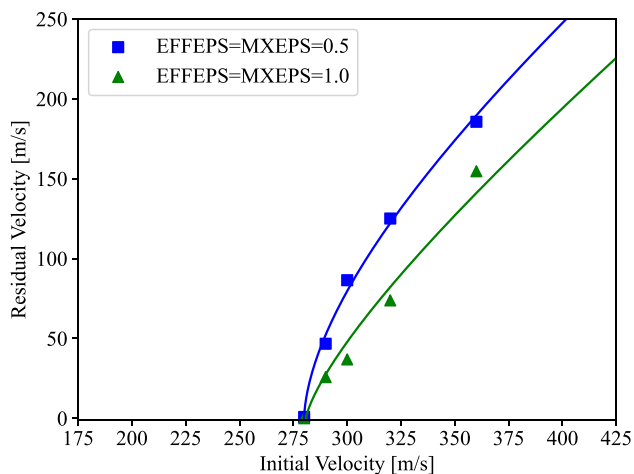


Fig. 20 Ballistic limit curves for parameter study on erosion criteria in the 3D model

Table 10 Results from numerical simulations when striking reinforcement with $v_i = 300$ m/s

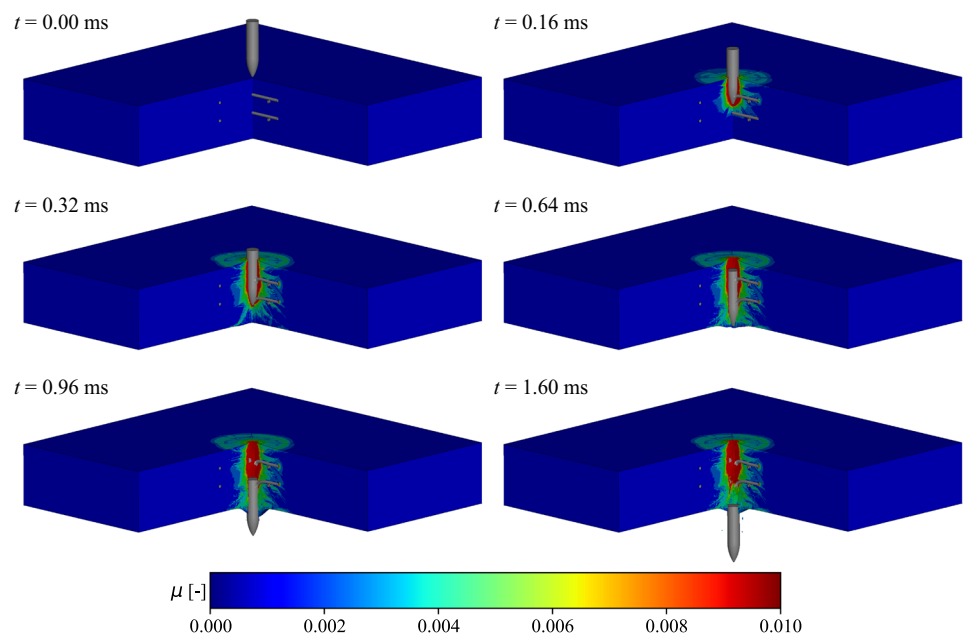
Slab type	D_{rebar} [mm]	No. elems. along rebar diameter	Numerical	Experimental
			v_r [m/s]	v_r [m/s]
	(D_{rebar}/D_p)			
UA	–	–	36.8	62.5
A2	5 (0.20)	10	75.3	41.0
–	6 (0.30)	12	31.6	–
A1	7 (0.35)	14	0.0	11.8
–	8 (0.40)	16	0.0	–

Discussion

It is known from the literature that the tensile strength is an important parameter for ballistic resistance for both thin and thick concrete slabs [15, 33, 55]. The three strength parameters f_c , f_{cc} and f_t of the concrete were found using standardised material tests performed 28 days post casting. The impact tests were performed 31 to 37 days post casting, resulting in a possible underestimation of the strength parameters. Consequently, the ballistic limit velocity v_{bl} of the slabs might have been slightly underestimated in the FE simulations. Furthermore, the tensile strength of the concrete was found from tensile splitting tests. These tests have been claimed to underestimate the tensile capacity of the concrete [56], leading to another possibility of underestimation of v_{bl} in the FE simulations. Additionally, the different curing conditions for the material specimens and the slabs might have lead to different compaction behaviour. Experimental studies have shown that there is a significant influence on the triaxial behaviour from the water saturation ratio [57] of the concrete. This effect is most prominent for high confinement. However, very few elements in the simulations showed pressure levels above 400 – 500 MPa, and we would thus assume that these effects did not affect the results significantly.

The porosity of the concrete can have significant effects on the triaxial compression behaviour, and can affect ballistic performance [58, 59]. When a concrete is not vibrated after casting, there is a possibility of entrapped air porosity in the structure. Vibrating was not performed for the concrete in this study, leading to possible effects on the porosity. As one point of the study was to calibrate the material model

Fig. 21 Volumetric strain for reinforced slab with rebar diameter 5 mm. $v_i = 300$ m/s, $v_r = 75.3$ m/s. Slab A2-8 from experiments: $v_i = 301.6$ m/s and $v_r = 41.0$ m/s



based on simple material tests, we have not tried to quantify the porosity of the concrete.

Adding reinforcement in concrete slabs is a way of increasing the tensile capacity of the structure. Thus, adding reinforcement should be a way of increasing the impact resistance of the concrete slabs. However, from the experiments performed in this study, it was seen that adding grid steel reinforcement did not affect v_{bl} significantly when projectiles did not hit the rebars. These results are similar to results in the literature [2, 3, 17]. Two effects of adding reinforcement were observed in this study. First, it was observed that the reinforcement trapped fragments in some of the component tests, thus reducing the amount of debris that detached from the back of the slabs. Similar to studies by Lee et al. [9] and Rajput and Iqbal [18], it seemed that the possibility of fragment trapping increased when the rebar spacing was reduced. The other effect observed for the reinforced slab sets was that when a projectile struck the reinforcement during perforation, the residual velocity was lower compared to not striking the reinforcement. This effect was observed for the bars with diameter 7 mm, but not for diameter 5 mm, suggesting that the perforation resistance when striking the reinforcement is affected by the diameter of the rebar, contrary to the findings of Lee et al. [9]. The ratio D_{rebar}/D_p could also be of importance when striking the reinforcement, and might explain the difference in results compared to the results in [9]. However, for the slabs in this study, it is difficult to conclude whether this effects stems from the inherit scatter in the data. Hanchak et al. [2] found that striking reinforcement had negligible effect on the ballistic resistance for thicker slabs than those used herein and for initial velocities v_i two times v_{bl} . For the projectiles striking the rebar in this study, v_i was less than 10 % larger than v_{bl} , showing that the significance of striking the reinforcement might also be affected by the ratio v_i/v_{bl} .

The shear modulus G , fracture parameters α and β , and hardening parameters B and N for the concrete were found using an inverse modelling procedure of a cylinder compression test in LS-OPT. The experimental engineering stress–strain curves were found using 2D-DIC and subsequently used as target curves for the inverse modelling. The numerical model provided good results for the cylinder compression test and the results were validated against a cube compression test in a 3D model. Neither model included the post-peak behaviour, mainly because the deformations cannot be reasonably assumed to be homogeneous post peak. The description of the post-peak behaviour might be important in perforation simulations, especially when high levels of confinement appear. Additionally, as reported by Antoniou et al. [5], triaxial compression tests are needed if a proper description of the pressure hardening is needed.

Table 9 compares v_{bl} and Recht-Ipson parameters for the plain slabs. The MHJC model provided good agreement

between experiments and FE simulations. The ballistic limit velocity found using the 3D model was only 1% higher than the experimental value, yielding slightly non-conservative results. For higher initial velocities, the 3D results and experimental results were in good agreement. The results from the 2D model were conservative, with v_{bl} 6 % lower than the experimental value, i.e., lower accuracy than the 3D model. One reason that the 2D model has lower resistance might be related to element erosion in the models. Eroding/deleting an axisymmetric element is equivalent to eroding an entire torus of elements when we rotate about the symmetry axis, which in turn could reduce the resistance. Typical simulation times for the 2D model were 2-3 min, and 10-29 h for the 3D model. Thus, the 2D model is well suited in engineering purposes and numerical assessments in the design phase of concrete protective structures.

In the parameter study, it was seen that doubling f_c resulted in a 19.2 % increase in v_{bl} , while doubling f_t resulted in an increase of 5.8 %. This suggests that f_c has a larger effect on the ballistic limit velocity than f_t , contrary to the findings of Kristoffersen et al. [33]. They found that f_t had a greater influence on v_{bl} than f_c for 50 mm thick slabs, with the same type of projectile as used in this study. Li et al. [21] found experimentally that tensile damage is more important for thinner slabs, while thick slabs will have strong influence on compaction during perforation. When comparing the results from Kristoffersen et al. [33] and the results in this study, the same phenomena is observed, and this might thus explain the increased effect of f_c on v_{bl} in this study. This is also in line with the numerical results presented by Shiu et al. [19], where the influence of compaction increased with slab thickness.

Regarding the strain-rate formulation in MHJC material model, Polanco-Loria et al. [32] modified the original strain-rate function to avoid negative rate enhancement predicted by the HJC model for low strain rates. In 2018, Johnson et al. [60] argued that new experimental data showed that the strain-rate enhancement effects in concrete were greater than previously determined for the HJC model. When compared to material data available in the literature [61] for different concrete types, we see that the non-linear formulation with $C = 0.04$ as used by Polanco-Loria et al. [32] provides reasonable results.

Element erosion is a commonly used technique in FE simulations. Applying erosion criteria to erode/delete elements that have undergone severe deformation to ensure computational efficiency is not correct in a physical sense, however, these elements are considered to have little to no effect further in the simulation. Nevertheless, it is interesting to study how the application of such a numerical feature affects the ballistic results. The parameter study on erosion criteria showed slightly different results compared to the 3D reference model. Decreasing the values of EFFEPS and

MXEPS from 1.0 to 0.5 resulted in a decrease in residual velocities above the ballistic limit. This shows that erosion parameters can be tuned to adjust the numerical perforation resistance, and for example provide conservative results if wanted by the user. By applying the same values in both the 2D and 3D models, the numerical description is consistent, which is important for comparison.

FE simulations with different reinforcement diameters showed that the impact resistance was affected by the reinforcement diameter when striking the reinforcement. The residual velocity of the projectile decreased as the rebar diameter increased when the initial velocity was kept constant. Increasing the rebar diameter to 7 and 8 mm even completely stopped the projectile. However, for the smallest simulated rebar diameter (5 mm), the projectile unexpectedly perforated the slab with a higher residual velocity compared with the plain concrete slab. We emphasise that the rebar diameter was the only parameter that was varied between the simulations of reinforced slabs – even the element size of all rebar diameters were the same. This result warrants further investigation, and we speculate that small rebar diameters may cause more localised deformation and thereby cracking directly behind the steel, which results in higher residual velocity.

Conclusions

From the experimental work performed in this study, the following conclusions can be drawn:

- Digital image correlation successfully estimated the engineering stress–strain relation for the commercially produced concrete.
- In the component tests, the scabbing area was generally larger than the spalling area. Fragmentation from the scabbing area occurred for all slabs, despite perforation not occurring for all cases.
- No clear effect on the ballistic parameters was found when adding reinforcement. However, fragment trapping was observed for some of the reinforced slabs. This effect seemed to increase when the spacing of the rebars was reduced, and the mass loss decreased for closer reinforcement spacing. When striking the reinforcement, the results indicated that the ballistic resistance increased with increasing rebar diameter. It is difficult to conclude whether or not this was caused by scatter in the ballistic data.

Both 2D and 3D finite element models were created using a modified version of the Holmquist-Johnson-Cook model to represent the material in the simulations of the impact tests.

From the numerical results, the following conclusions can be drawn:

- Parameters for the MHJC model were found from standardised material tests, from inverse modelling, and from the literature. Using the calibrated material constants and reasonable assumptions, good predictions of the ballistic limit velocities were obtained using both a 2D axisymmetric model and a 3D solid model of the concrete slab.
- The axisymmetric model was efficient and thus well suited for engineering approaches. A parameter study revealed that the inclusion of strain-rate effects in the phenomenological material model applied in this study is important to have decent results from the numerical simulations. Also, both the compressive and tensile strength affected the ballistic resistance of the slabs. However, a larger influence was found for the compressive strength for the slabs investigated in this study. FE simulations where projectiles struck the reinforcement bars revealed that the ballistic perforation resistance was affected by the reinforcement diameter.
- The calibration and implementation of the MHJC model is relatively simple, and it remains a reliable alternative to other concrete models where significantly more material parameters are required.

Acknowledgements The work in this study has been carried out with financial support from the Centre for Advanced Structural Analysis (CASA), Centre for Research-based Innovation, at the University of Science and Technology (NTNU), the Norwegian Defence Estates Agency (NDEA), and the Research Council of Norway through project no. 237885 (CASA). The authors would also like to extend our gratitude towards Mr. Vetle S. Gjesdal, Mr. Trond Auestad, Mr. Per Ø. Nordtug and Mr. Steinar Seehuus for assistance with the various experimental works.

Funding Open access funding provided by NTNU Norwegian University of Science and Technology (incl St. Olavs Hospital - Trondheim University Hospital).

Declarations

Conflict of interest The authors declare that they have no known competing financial interests or personal relationships that could have appeared to influence the work reported in this paper.

Open Access This article is licensed under a Creative Commons Attribution 4.0 International License, which permits use, sharing, adaptation, distribution and reproduction in any medium or format, as long as you give appropriate credit to the original author(s) and the source, provide a link to the Creative Commons licence, and indicate if changes were made. The images or other third party material in this article are included in the article's Creative Commons licence, unless indicated otherwise in a credit line to the material. If material is not included in the article's Creative Commons licence and your intended use is not permitted by statutory regulation or exceeds the permitted use, you will need to obtain permission directly from the copyright holder. To view a copy of this licence, visit <http://creativecommons.org/licenses/by/4.0/>.

References

1. Gagg CR (2014) Cement and concrete as an engineering material: an historic appraisal and case study analysis. *Eng Fail Anal* 40:114–140. <https://doi.org/10.1016/j.engfailanal.2014.02.004>
2. Hanchak SJ, Forrestal MJ, Young ER, Ehrgott JQ (1992) Perforation of concrete slabs with 48 MPa (7 ksi) and 140 MPa (20 ksi) unconfined compressive strengths. *Int J Impact Eng* 12(1):1–7. [https://doi.org/10.1016/0734-743X\(92\)90282-X](https://doi.org/10.1016/0734-743X(92)90282-X)
3. Dancygier AN, Yankelevsky DZ, Jaegermann C (2007) Response of high performance concrete plates to impact of non-deforming projectiles. *Int J Impact Eng* 34(11):1768–1779. <https://doi.org/10.1016/j.ijimpeng.2006.09.094>
4. Wu H, Fang Q, Chen XW, Gong ZM, Liu JZ (2015) Projectile penetration of ultra-high performance cement based composites at 510–1320 m/s. *Constr Building Mater* 74:188–200. <https://doi.org/10.1016/j.conbuildmat.2014.10.041>
5. Antoniou A, Daudeville L, Marin P, Omar A, Potapov S (2018) Discrete element modelling of concrete structures under hard impact by ogive-nose steel projectiles. *Eur Phys J Special Top* 227(1):143–154. <https://doi.org/10.1140/epjst/e2018-00059-y>
6. Kristoffersen M, Pettersen JE, Aune V, Børvik T (2018) Experimental and numerical studies on the structural response of normal strength concrete slabs subjected to blast loading. *Eng Struct* 174:242–255. <https://doi.org/10.1016/j.engstruct.2018.07.022>
7. Li Yang, Aoude Hassan (2020) Influence of steel fibers on the static and blast response of beams built with high-strength concrete and high-strength reinforcement. *Eng Struct* 221:111031. <https://doi.org/10.1016/j.engstruct.2020.111031>
8. Lee MJ, Kwak HG, Park GK (2021) An improved calibration method of the K & C model for modeling steel-fiber reinforced concrete. *Compos Struct* 269:114010. <https://doi.org/10.1016/j.compstruct.2021.114010>
9. Lee S, Kim C, Yu Y, Cho JYI (2021b) Effect of reinforcing steel on the impact resistance of reinforced concrete panel subjected to hard-projectile impact. *Int J Impact Eng* 148:103762. <https://doi.org/10.1016/j.ijimpeng.2020.103762>
10. Kristoffersen M, Hauge KO, Minoretti A, Børvik T (2021) Experimental and numerical studies of tubular concrete structures subjected to blast loading. *Eng Struct* 233:111543. <https://doi.org/10.1016/j.engstruct.2020.111543>
11. Rajput A, Iqbal MA, Gupta NK (2018) Ballistic performances of concrete targets subjected to long projectile impact. *Thin-Walled Struct* 126:171–181. <https://doi.org/10.1016/j.tws.2017.01.021>
12. Dancygier AN (1997) Effect of reinforcement ratio on the resistance of reinforced concrete to hard projectile impact. *Nucl Eng Des* 172(1):233–245. [https://doi.org/10.1016/S0029-5493\(97\)00055-1](https://doi.org/10.1016/S0029-5493(97)00055-1)
13. Dancygier AN, Yankelevsky DZ (1996) High strength concrete response to hard projectile impact. *Int J Impact Eng* 18(6):583–599. [https://doi.org/10.1016/0734-743X\(95\)00063-G](https://doi.org/10.1016/0734-743X(95)00063-G)
14. Wan W, Yang J, Xu G, Liu Y (2021) Determination and evaluation of Holmquist-Johnson-Cook constitutive model parameters for ultra-high-performance concrete with steel fibers. *Int J Impact Eng* 156:103966. <https://doi.org/10.1016/j.ijimpeng.2021.103966>
15. Liu J, Wu C, Su Y, Li J, Shao R, Chen G, Liu Z (2018) Experimental and numerical studies of ultra-high performance concrete targets against high-velocity projectile impacts. *Eng Struct* 173:166–179. <https://doi.org/10.1016/j.engstruct.2018.06.098>
16. Kamal IM, Eltehwewy EM (2012) Projectile penetration of reinforced concrete blocks: test and analysis. *Theor Appl Fract Mech* 60(1):31–37. <https://doi.org/10.1016/j.tafmec.2012.06.005>
17. Abdel-Kader M, Fouda A (2014) Effect of reinforcement on the response of concrete panels to impact of hard projectiles. *Int J Impact Eng* 63:1–17. <https://doi.org/10.1016/j.ijimpeng.2013.07.005>
18. Rajput A, Iqbal MA (2017) Impact behavior of plain, reinforced and prestressed concrete targets. *Mater Des* 114:459–474. <https://doi.org/10.1016/j.matdes.2016.10.073>
19. Shiu W, Donze F, Daudeville L (2008) Compaction process in concrete during missile impact: a DEM analysis. *Comput Concr* 5:329–342. <https://doi.org/10.12989/cac.2008.5.4.329>
20. YADE. Open Source Discrete Element Code. Václav Šmilauer, <http://yade.wikia.com/wiki/Yade>, (2004)
21. Li PP, Brouwers HJH, Qingliang Yu (2020) Influence of key design parameters of ultra-high performance fibre reinforced concrete on in-service bullet resistance. *Int J Impact Eng* 136:103434. <https://doi.org/10.1016/j.ijimpeng.2019.103434>
22. Lu Y, Song Z, Tu Z (2010) Analysis of dynamic response of concrete using a mesoscale model incorporating 3D effects. *Int J Prot Struct* 1(2):197–218. <https://doi.org/10.1260/2041-4196.1.2.197>
23. Ren H, Rong Y, Xu X (2021) Mesoscale investigation on failure behavior of reinforced concrete slab subjected to projectile impact. *Eng Fail Anal* 127:105566. <https://doi.org/10.1016/j.engfailanal.2021.105566>
24. Riedel W, Thoma K, Hiermaier S, Schmolinske E (1999) Penetration of reinforced concrete by BETA-B-500 numerical analysis using a new macroscopic concrete model for hydrocodes. In Proceedings of the 9th International Symposium on the Effects of Munitions with Structures, vol. 315. Berlin-Strausberg Germany
25. Pavlovic A, Fragassa C, Disic A (2017) Comparative numerical and experimental study of projectile impact on reinforced concrete. *Compos Part B: Eng* 108:122–130. <https://doi.org/10.1016/j.compositesb.2016.09.059>
26. Holmquist TJ, Johnson GR, Cook WH (1993) A computational constitutive model for concrete subjected to large strains, high strain rates and high pressures. Proceedings of 14th international symposium on Ballistics, Quebec, Canada., pp 591–600
27. Smith M (2009) ABAQUS/Standard User's Manual, Version 6.9. Dassault Systèmes Simulia Corp, Johnston
28. LS-DYNA. LS-DYNA Keywords User's Manual - Volume I. Livermore Software Technology (LST) An Ansys Company, (2020)
29. Levi-Hevroni D, Kochavi E, Kofman B, Gruntman S, Sadot O (2018) Experimental and numerical investigation on the dynamic increase factor of tensile strength in concrete. *Int J Impact Eng* 114:93–104. <https://doi.org/10.1016/j.ijimpeng.2017.12.006>
30. Antoniou A, Børvik T, Kristoffersen M (2023) Evaluation of automatic versus material test-based calibrations of concrete models for ballistic impact simulations. *Int J Prot Struct*. <https://doi.org/10.1177/20414196231164431>
31. Akshaya Gomathi K, Rajagopal A, Reddy KSS, Ramakrishna B (2020) Plasticity based material model for concrete subjected to dynamic loadings. *Int J Impact Eng* 142:103581. <https://doi.org/10.1016/j.ijimpeng.2020.103581>
32. Polanco-Loria M, Hopperstad OS, Børvik T, Berstad T (2008) Numerical predictions of ballistic limits for concrete slabs using a modified version of the HJC concrete model. *Int J Impact Eng*. <https://doi.org/10.1016/j.ijimpeng.2007.03.001>
33. Kristoffersen M, Toreskås OL, Dey S, Børvik T (2021) Ballistic perforation resistance of thin concrete slabs impacted by ogive-nose steel projectiles. *Int J Impact Eng* 156:103957. <https://doi.org/10.1016/j.ijimpeng.2021.103957>
34. Fagerholt E (2017) eCorr v4.0 Documentation. NTNU, Norway. Cited on 03.06.21. <https://folk.ntnu.no/egilf/ecorr/doc/>
35. Livermore Software Technology (LST). LS-OPT® User's Manual. ANSYS, (2019)

36. Børvik T, Langseth M, Hopperstad OS, Malo KA (1999) Ballistic penetration of steel plates. *Int J Impact Eng* 22(9):855–886. [https://doi.org/10.1016/S0734-743X\(99\)00011-1](https://doi.org/10.1016/S0734-743X(99)00011-1)
37. Ren F, Mattus CH, Wang JJ-A, DiPaolo BP (2013) Effect of projectile impact and penetration on the phase composition and microstructure of high performance concretes. *Cem Concr Compos* 41:1–8. <https://doi.org/10.1016/j.cemconcomp.2013.04.007>
38. Toni Technik GMBH. Load Frame for Compressive Strength Tests - Model 2031. Toni Technik GMBH, [Online] Cited On 22.12.21, (2021). URL <https://tonitechnik.com/product/load-frame-for-compressive-strength-tests-model-2031/>
39. The European Committee for Standardization (CEN). Eurocode 2: Design of concrete structures Part 1.1: General rules and rules for buildings. The European Committee for Standardization, (2018)
40. FIB/CEB. High performance concretes, A state-of-the-art report. Strategic Highway Research Program - National Research Council, Switzerland, (1990)
41. Instron. 5980 SERIES Universal Testing Systems up to 600 kN Force Capacity. Instron US, 2020. URL <https://www.instron.us/products/testing-systems/universal-testing-systems/high-force-universal-testing-systems/5980-series-floor-models>
42. Screening Eagle Technologies. Proceq Products. Screening Eagle Technologies, 2021. URL <https://www.screeningeagle.com/en/products/proceq-gp8000>
43. Teng TL, Chu YA, Chang FA, Chin HS (2005) Numerical analysis of oblique impact on reinforced concrete. *Cem Concr Compos* 27(4):481–492. <https://doi.org/10.1016/j.cemconcomp.2004.05.005>
44. Goldsmith W (1999) Non-ideal projectile impact on targets. *Int J Impact Eng* 22(2):95–395. [https://doi.org/10.1016/S0734-743X\(98\)00031-1](https://doi.org/10.1016/S0734-743X(98)00031-1)
45. Chen XW, Fan SC, Li QM (2004) Oblique and normal perforation of concrete targets by a rigid projectile. *Int J Impact Eng* 30(6):617–637. <https://doi.org/10.1016/j.ijimpeng.2003.08.003>
46. Recht RF, Ipson TW (1960) Ballistic perforation dynamics. *J Appl Mech, Trans ASME* 30(3):384–390. <https://doi.org/10.1115/1.3636566>
47. Baltay P, Gjelsvik A (1990) Coefficient of friction for steel on concrete at high normal stress. *J Mater Civ Eng* 2(1):46–49. [https://doi.org/10.1061/\(ASCE\)0899-1561\(1990\)2:1\(46\)](https://doi.org/10.1061/(ASCE)0899-1561(1990)2:1(46))
48. Hopperstad OS, Børvik T (2020) Impact Mechanics - Part 1: Modelling of plasticity and failure with explicit finite element methods. SIMLab, NTNU
49. Børvik T, Dey S, Clausen AH (2009) Perforation resistance of five different high-strength steel plates subjected to small-arms projectiles. *Int J Impact Eng* 36(7):948–964. <https://doi.org/10.1016/j.ijimpeng.2008.12.003>
50. Cockcroft MG, Latham DJ (1968) Ductility and the workability of metals. *J Inst Met* 96:33–39
51. Ruggieri C, Panontin TL, Dodds RH (1990) Numerical modeling of ductile crack growth in 3-D using computational cell elements. *Int J Fract* 82(1):67–95. <https://doi.org/10.1007/BF00017864>
52. Georjgin JF, Reynouard JM (2003) Modeling of structures subjected to impact: concrete behaviour under high strain rate. *Cem Concr Compos* 25(1):131–143. [https://doi.org/10.1016/S0958-9465\(01\)00060-9](https://doi.org/10.1016/S0958-9465(01)00060-9)
53. Saini D, Oppong K, Shafei B (2021) Investigation of concrete constitutive models for ultra-high performance fiber-reinforced concrete under low-velocity impact. *Int J Impact Eng* 157:103969. <https://doi.org/10.1016/j.ijimpeng.2021.103969>
54. Børvik T, Hopperstad OS, Berstad T, Langseth M (2001) A computational model of viscoplasticity and ductile damage for impact and penetration. *Eur J Mech - A/Solids* 20(5):685–712. [https://doi.org/10.1016/S0997-7538\(01\)01157-3](https://doi.org/10.1016/S0997-7538(01)01157-3)
55. Riera JD (1989) Penetration, scabbing and perforation of concrete structures hit by solid missiles. *Nucl Eng Des* 115(1):121–131. [https://doi.org/10.1016/0029-5493\(89\)90265-3](https://doi.org/10.1016/0029-5493(89)90265-3)
56. Resan SF, Chassib SM, Zemam SK, Madhi MJ (2020) New approach of concrete tensile strength test. *Case Stud Constr Mater* 12:e00347. <https://doi.org/10.1016/j.cscm.2020.e00347>
57. Forquin P, Safa K, Gary G (2010) Influence of free water on the quasi-static and dynamic strength of concrete in confined compression tests. *Cem Concr Res* 40(2):321–333. <https://doi.org/10.1016/j.cemconres.2009.09.024>
58. Forquin P, Arias A, Zaera R (2008) Role of porosity in controlling the mechanical and impact behaviours of cement-based materials. *Int J Impact Eng* 35(3):133–146. <https://doi.org/10.1016/j.ijimpeng.2007.01.002>
59. Malecot Y, Zingg L, Briffaut M, Baroth J (2019) Influence of free water on concrete triaxial behavior: the effect of porosity. *Cem Concr Res* 120:207–216. <https://doi.org/10.1016/j.cemconres.2019.03.010>
60. Johnson G, Holmquist T, Gerlach C (2018) Strain-rate effects associated with the HJC concrete model. *EPJ Web of Conf - DYMAT 2018*:183. <https://doi.org/10.1051/epjconf/201818301008>
61. Bischoff PH, Perry SH (1991) Compressive behaviour of concrete at high strain rates. *Mater Struct* 24(6):425–450. <https://doi.org/10.1007/BF02472016>